Diplomarbeit

3D Reconstruction of the Human Rib Cage from 2D Projection Images Using a Statistical Shape Model

von Jalda Dworzak
eingereicht am 5. Dezember 2009

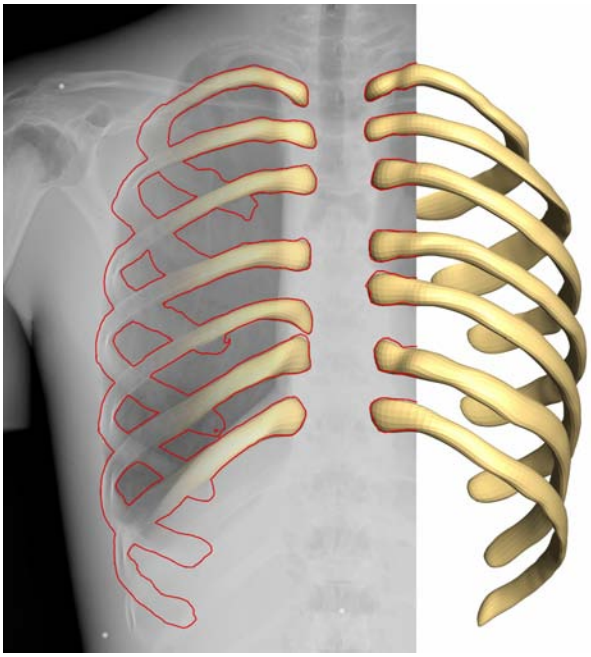

Technische Universität Berlin - Fakultät IV
Institut für Technische Informatik und Mikroelektronik
Computer Vision and Remote Sensing

&

Zuse-Institut Berlin (ZIB)
Visualisierung und Datenanalyse

Betreuer

Prof. Dr.-Ing. Olaf Hellwich, Technische Universität Berlin
Dr. Hans Lamecker, Zuse-Institut Berlin

Die selbständige und eigenhändige Anfertigung versichere ich an Eides Statt.

Berlin, 5. Dezember 2009

Abstract

This diploma thesis presents an approach for the three-dimensional (3D) shape and pose reconstruction of the human rib cage from few segmented two-dimensional (2D) projection images. The work is aimed at supporting temporal subtraction techniques of subsequently acquired radiographs by establishing a method for the assessment of pose differences in sequences of chest radiographs of the same patient. The reconstruction method is based on a 3D statistical shape model (SSM) of the rib cage, which is adapted to 2D projection images of an individual rib cage. To drive the adaptation, a distance measure is minimized that quantifies the dissimilarities between 2D projections of the 3D SSM and the 2D projection images. Different silhouette-based distance measures are proposed and evaluated regarding their suitability for the adaptation of the SSM to the projection images. An evaluation was performed on 29 sets of biplanar binary images (posterior-anterior and lateral) as well as on posterior-anterior X-ray images of a phantom of a human rib cage. Depending on the chosen distance measure, our experiments on the combined reconstruction of shape and pose of the rib cages yield reconstruction accuracies from 2.2 mm to 4.7 mm average mean 3D surface distance. Given a geometry of an individual rib cage, the rotational errors for the pose reconstruction range from 0.1° to 0.9°. In conclusion, the results show that the proposed method is suitable for the estimation of pose differences of the human rib cage in projection images. Thus, it is able to provide crucial 3D information for the registration during the generation of 2D subtraction images.

Deutsche Zusammenfassung

Im Rahmen dieser Diplomarbeit wurde ein Verfahren zur dreidimensionalen (3D) Rekonstruktion der Lage und Form des menschlichen Brustkorbes aus wenigen zweidimensionalen (2D) Projektionsbildern entwickelt und implementiert. Ziel der Arbeit ist es, durch die Bereitstellung einer Methode zur Ermittlung von 3D-Lageunterschieden zwischen zeitlich versetzt aufgenommenen Thoraxradiographien, diagnostische Bildsubtraktionsverfahren zu unterstützen und zu verbessern. Die Rekonstruktionsmethode basiert auf einem statistischen 3D-Formmodell (SFM) der Rippen, das zum Zwecke der Rekonstruktion in eine Bildebene projeziert und an die 2D-Bilddaten eines individuellen Brustkorbes angepasst wird. Diese Anpassung wird durch die Minimierung eines Distanzmaßes gesteuert, das Unterschiede zwischen Projektionen des SFMs und den 2D-Projektionsdaten misst. Hierfür wurden unterschiedliche Silhouetten-basierte Distanzmaße entwickelt und hinsichtlich ihrer Anwendbarkeit auf das Rekonstruktionsproblem ausgewertet. Eine Validierung des Verfahrens wurde mit Hilfe von 29 künstlich generierten Paaren biplanarer Binärbilder (Frontal- und Seitenansicht) sowie mit Radiographien (nur Frontalansicht) eines Thoraxmodells (Phantom) durchgeführt. Experimente zur gleichzeitigen Ermittlung von Form und Lage eines Brustkorbes erreichen, in Abhängigkeit des gewählten Distanzmaßes, eine Rekonstruktionsgenauigkeit zwischen 2.2 bis 4.7 mm mittlerer 3D-Oberflächendistanz. Ist die Form bereits vor der Anpassung bekannt, ergibt eine reine Lageabschätzung Rotationsfehler im Bereich von 0.1° bis 0.9°. Die Ergebnisse zeigen, dass die vorgeschlagene Methode für die Abschätzung von Lageunterschieden in Röntgenbildern des menschlichen Thorax geeignet ist. Folglich können mit Hilfe des Rekonstruktionsverfahrens entscheidende 3D-Information für die Generierung von 2D-Subtraktionsbildern, mit Anwendung in der computergestützten, medizinischen Diagnose, gewonnen werden.

Acknowledgements

On a first note of my diploma thesis, I want to express my gratitude to my supervisor Dr. Hans Lamecker whose work was the starting point and basis of this thesis and who provided me with indispensable support and feedback. My sincere thanks go to Prof. Dr.-Ing. Olaf Hellwich for his valuable advice and for allowing me to pursue my graduate work under his supervision.

I am indebted to Hans-Christian Hege who enabled me to work in the extremely resourceful environment of the Visualization an Data Analysis Group at the *Zuse-Institute Berlin* (ZIB). The pleasant and inspiring atmosphere created by all the members of my department is greatly appreciated. Furthermore, I want to thank Dr. Stefan Zachow who provided me with excellent guidance and in whose Medical Planning Group I learned a great deal about computer-aided surgery and diagnosis as well as medical image analysis.

I am especially grateful for the exceptional help and constant encouragement I received from my collegues Dagmar Kainmüller and Heiko Seim. Thank you for sharing your time on countless occasions and for being so patient with me!

The work of this thesis would not have been possible without the cooperation between the Department of Medical Imaging Systems at *Philips Research Europe* in Hamburg and the Visualization and Data Analysis Group at ZIB in Berlin. I am very much obliged to Dr. Jens von Berg, Dr. Cristian Lorenz, Tobias Klinder and Dennis Barthel for giving me the opportunity to work on such an exiting and application-oriented topic, for sharing their great expertise and making my stays in Hamburg fruitful and enjoyable. Further thanks go to Dr. Cornelia Schaefer-Prokop for providing the radiographs.

Last but definitely not least, I wish to thank my family and friends for their support.

Contents

List of Figures

1 Introduction

In this introductory chapter, an overview of the diploma thesis is provided. The purpose and aims of this work are stated, followed by a structural outline.

1.1 Motivation

In clinical routine, radiography is an inexpensive and frequently used imaging technique for screening and diagnosis of the chest region. However, interpreting radiographs is difficult, especially if conclusions about the 3D geometry need to be drawn. For this reason, computer-aided diagnosis (CAD) methods are developed and increasingly applied to support physicians [vGtHRV01].

A widely used diagnosis method is to compare current chest radiographs with previously acquired radiographs of the same patient to detect changes in the health status. This approach is also commonly used in the context of interval studies, where radiographs are acquired intermittently to identify *interval changes* between subsequent images to observe the course of a disease, e.g., tumor growth. To detect interval changes by automated procedures, a CAD method known as *temporal image subtraction* can be applied [KDM+94]. A subtraction image shows the difference between a previous and a follow up image of a patient (cf. Fig. 1.1(a)) after a suitable image registration, i.e., an optimal mapping via geometrical transformation of one image to another such that objects in the images are spatially matched. Ideally, unchanged anatomical structures are eliminated while any interval change caused by new opacities (e.g. tumors) appears strongly contrasted and stands out more clearly. Studies on the benefit of temporal subtraction verify a significant improvement in the detection accuracy of abnormalities in the chest region in case subtraction images are used [KKH+06]. One major problem for the generation of suitable subtraction images is the deviation of the patient's pose between subsequent images. For this reason, image registration prior to the image subtraction is indispensable, since the imaging geometry may differ for each radiograph.

In case the registration fails due to major pose differences, undesired artifacts emerge that might superimpose the interval change. In consequence, the interval change may remain undetected (see Fig. 1.1(b)). The quality of subtraction images is especially impaired, if the patient leans forwards or backwards (anterior-posterior (AP) inclination) or rotates around his main body axis [KDM+94]. The compensation of such 3D pose differences using 2D to 2D image registration does not necessarily lead to sufficient results.

A phantom study of von Berg et al. [vBMSPN08] showed that deformable 2D to 2D image registration, compared to non-deformable registration, better compensates for 3D pose differences. The range of pose difference, still allowing faithful detection of interval changes from image pairs, is increased up to 2.3° using their registration method. Beyond that, it is desirable to further enhance the registration, to allow

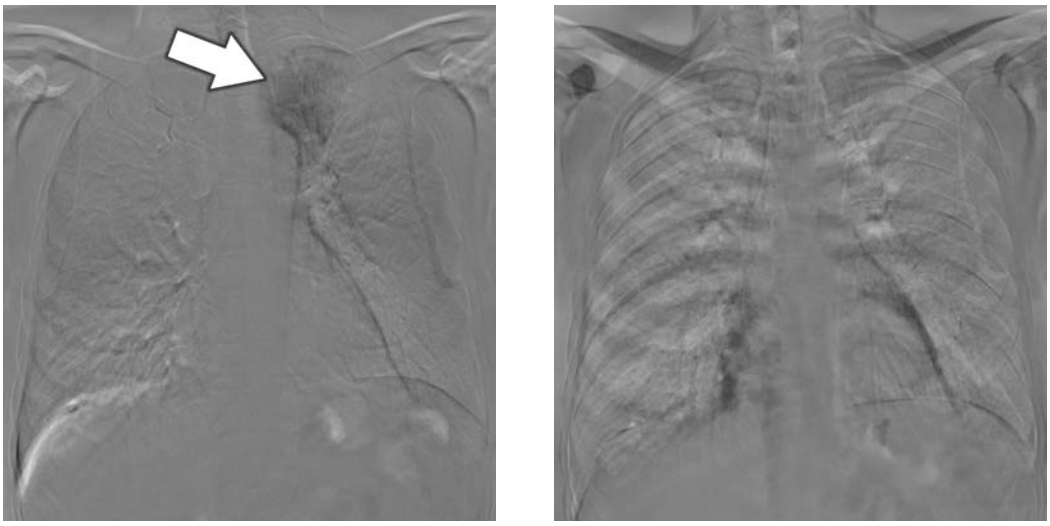

(a) (b)

Figure 1.1: Two different subtraction images of the same patient after image registration: (a) The interval change (the development of pneumonia) is clearly visible (arrow). (b) No interval change is detectable due to artifacts that are caused by a strong anterior-posterior inclination.

for image subtraction despite a high 3D pose difference. An accurate assessment of this 3D pose difference, which causes the discrepancies between two images, can provide valuable information. This 3D information can be used to improve the image subtraction in cases where current deformable registration methods, which rely on 2D information only, are likely to fail.

1.2 Problem and Objectives

This work aims at supporting temporal subtraction techniques of subsequently acquired radiographs by establishing a method to assess 3D pose differences between pairs of chest radiographs of the same patient. To quantify the 3D pose difference between a pair of images, the 3D pose of the patient's thorax during image acquisition needs to be estimated from the respective images. Such *3D pose reconstructions* require structures within the radiographs that allow for a reliable estimation of their respective 3D pose throughout different images. Note that these images can be acquired with considerable time intervals of month or even years. The choice of a suitable anatomical structure should be made bearing in mind that, for example, soft tissue undergoes deformation (e.g. due to respiration) or the posture of the patient's limbs varies independently from the thorax.

In this work, the use of the rib cage is proposed to infer the 3D pose of a patient's thorax from 2D images. The ribs are suitable to serve for this task: They are rigid structures that do not change their shape notably over time. In comparison to scapulae and clavicle (cf. Fig. 2.1), their pose is largely independent from the arm posture. Another important argument is that ribs are reasonably contrasted in radiographs. Hence, they can be used as a reference system to define pose differences

of a patient between time intervals (see Fig. 1.2).

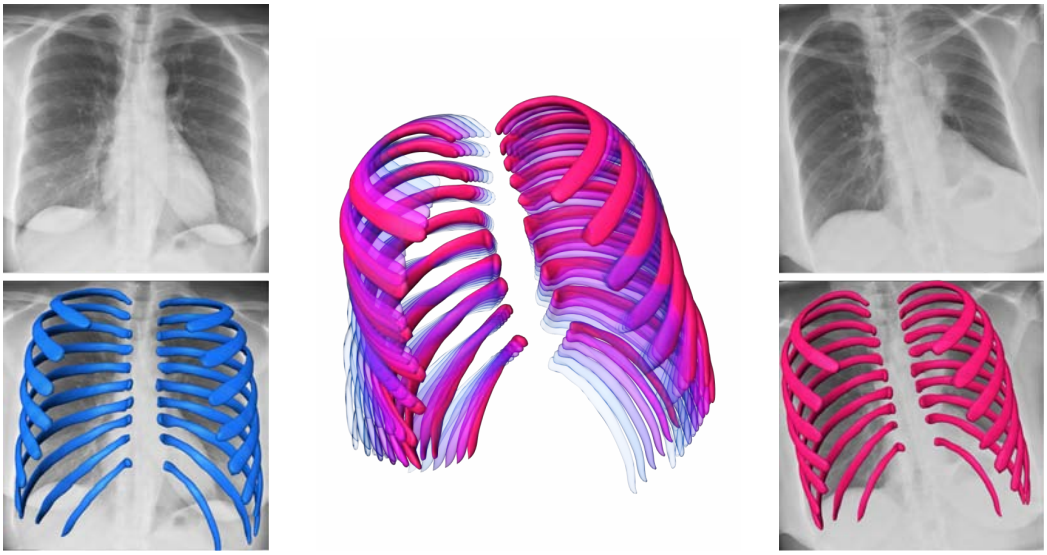

Figure 1.2: Two X-ray images of the same patient show considerable differences due to a variation of the patient's pose (top, left and right). The transformation between two 3D rib cage models, which are the outcome of the 3D pose reconstructions from each image (bottom, left and right), indicates the 3D pose difference to be determined (center).

The general idea of the proposed 3D pose reconstruction method is to match the patient's individual 3D rib cage model to the image data such that the pose of the 3D model yields a good approximation of the patient's pose during image acquisition. This approach, however, assumes that a virtual representation of the patient's individual rib cage is available. In practice this is rarely the case, which means that the patient-specific rib cage geometry needs to be retrieved first. Therefore this work addresses two problems:

1. **3D shape reconstruction:** The 3D geometry of the rib cage needs to be estimated from patient-specific data. Here, a 3D reconstruction from few 2D images is a valuable alternative to an expensive acquisition of tomographic image data with higher radiation exposure for the patient.

2. **3D pose reconstruction:** The patient's individual 3D rib cage, reconstructed previously, is used to recover the 3D pose from subsequent 2D images of the respective patient. The relative position and orientation of the rib cage with regard to a given image acquisition setup is estimated.

The problem of reconstructing objects from image data appears in numerous areas ranging from medical image analysis to computer vision. In most applications, objects need to be retrieved that are of the same dimension as the image data. The general task of reconstructing projective data, as in our case the 3D reconstruction of anatomical structures from 2D X-ray images, is challenging as only partial information is available. A 3D reconstruction from 2D projections attempts to reverse many-to-one mappings of 3D points to 2D space. This introduces ambiguity, since the projection of a point in 2D can be mapped back to multiple points in 3D. Thus,

the problem is generally ill-posed. A factor that limits the information at hand even more is the small number of X-ray images to be used for a 3D reconstruction. In clinical standard examinations, two radiographs, a frontal view (posterior-anterior) and a side view (lateral) are acquired. Thus, a method should require two images at most to be universally applicable. There are even advantages to use only one image, which will be discussed in Sect. 2.4.

In order to render the problem of 3D estimation from projection images well-posed, suitable 3D information has to be introduced into the reconstruction process. For this reason, a model-based approach using a 3D statistical shape model (SSM) as a template is chosen. The 3D SSM provides essential a-priori knowledge about the shape to be reconstructed.

A difficulty involved in a 3D reconstruction from X-ray images is that the reconstruction process relies on the detection of features that represent the anatomy in the X-ray images. Extracting these features is a challenging task in itself and strongly depends on the details of the imaging protocol. In this work, it is assumed that the ribs can be segmented from X-ray images. In most situations this assumption is true, i.e., rib boundaries can be identified visually in X-ray images and, at least, outlined manually. Work to extract the contours of the ribs from frontal X-ray images has been reported [vGtHR00, YGA95, LvG06, PCD06, PJW03]. Nevertheless, the automation of this task is still an open research problem not being within the scope of this work.

The objective of this work is to devise methods for the 3D reconstruction of shape and pose from rib silhouettes in 2D projection images based on an SSM. The goal is to show that the proposed reconstruction method yields feasible results within a well-defined experimental setup, and thus provides a solid basis for future clinical applications. Artificial projection images of the rib cage, for which the exact parameters to be reconstructed are known, enable us to verify the accuracy of the reconstruction results.

1.3 Contribution

This work is based on the method of Lamecker et al. [LWH06], which uses a 3D SSM for the reconstruction of complex 3D *shapes* from 2D projection images. It has been validated with geometries of the pelvic bone. In this thesis their method is extended and adapted to the outlined problem above; the reconstruction of rib cages. The method is extended in two directions:

1. Besides reconstructions of shapes, 3D *pose* reconstructions with respect to a known image acquisition setup are implemented. This is crucial for shape reconstructions in a more realistic (clinical) setting and for supporting temporal subtraction techniques as described above.

2. The distinct and complex geometry of the rib cage is considered. Here, new problems arise which call for new solutions compared to the case of the pelvic bone geometry [LWH06].

The general idea and main components of the reconstruction method are illustrated in Fig. 1.3. The approach achieves reconstructions of the rib cage by matching a

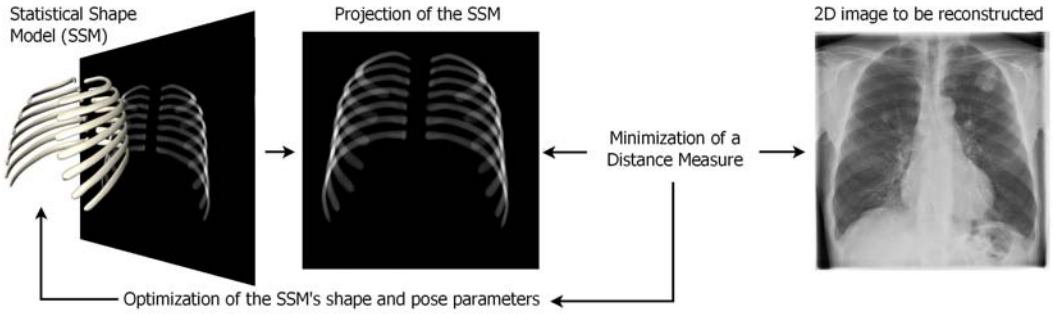

Figure 1.3: The general idea of the reconstruction scheme: Projections of the SSM are generated and compared to the 2D projection images by means of a distance measure. By employing an optimization process, parameters of the SSM are iteratively adapted such that the distance measure is minimized and the similarity between the projections (SSM and patient) is increased.

3D template shape (an SSM) to 2D projections of the individual rib cage to be reconstructed. To this end, *projections of the SSM* are generated (*model images*) and compared to the 2D images of the rib cage (*reference images*) on the basis of image features, e.g., contours of rib boundaries. Dissimilarities of the model images to the reference images are iteratively reduced by adapting parameters of the SSM that control its 3D pose (and 3D shape) variations. To drive the adaptation, a *distance measure* is minimized that quantifies the dissimilarities between the model images and the reference images. The adapted 3D SSM then yields an approximation of the patient's individual rib cage geometry at the time of obtaining the reference images.

In this work, different edge-based distance measures are compared with regard to their application to the 3D reconstruction of the rib cage. The accuracy of pose reconstructions from one and from two calibrated projection images is evaluated. Such an evaluation has not been done with other related rib reconstruction methods before. The evaluation is performed on artificial, binary projection images, as well as on *real* radiographs of an artificially modeled human thorax containing real thoracic bones (phantom). In addition, exemplary pose reconstructions from *clinical* X-ray images are provided. The experiments on real radiographs intend to validate the reconstruction method with respect to the intended CAD-application.

In this thesis, it will be shown that a 3D reconstruction of shape and pose can be achieved from segmented projection images of the rib cage. A 3D shape reconstruction (including the recovery of the pose) can be performed with an average accuracy of 2.2 to 4.5 mm 3D surface distance. Furthermore, if the shape is known, the pose alone can be accurately estimated even from a single projection (with rotation errors $\leq 0.4°$).

Parts contained in this thesis have been published in a more concise and reviewed contribution [DLvB+09]. The experimental results therein only include the evaluation using binary projections.

The implementation of this work was realized in C++ as an extension to the visualization framework Amira [ZA], which is developed at the *Zuse-Institute Berlin* (ZIB).

1.4 Overview

In this section, the outline of this thesis and a brief overview of each chapter is given.

Medical Background This chapter introduces and illustrates relevant anatomical terms associated with the anatomy of the human rib cage. It describes the characteristics of chest radiographs and provides background information on temporal subtraction techniques. Afterwards, requirements for a rib cage reconstruction system are derived.

Related Work Existing methods related to 2D/3D reconstruction problems are described and compared. They either specifically address the reconstruction of the rib cage or they are methodically related to our work by dealing with model-based 3D pose or shape reconstruction from 2D projection images.

SSM-based Geometry Reconstruction from 2D Projection Images This chapter introduces the most important methodical ingredients for a 3D reconstruction from 2D projection images, following the 3D shape reconstruction approach of Lamecker et al. [LWH06]. An overview of how these components interact during the reconstruction process is given.

3D Reconstruction of the Human Rib Cage from X-ray Images The approach for the 3D pose and shape reconstruction of the human rib cage from projection images is described. The description focuses on different distance measures that are adapted to the particular needs of the demanding geometry of the rib cage. Strategies to find a suitable initialization are considered.

Experiments and Results In the first part of this chapter, findings that led to the choice of appropriate distance measures are presented. The second part of the chapter focuses on experiments to assess the reconstruction accuracy using different distance measures to reconstruct the pose of a rib cage as well as its shape from one or two projection images. Finally, the quality of the method regarding the intended CAD-application is tested on real radiographs.

Discussion and Future Work The results and implications for the applicability of the rib cage reconstruction method to assess pose differences between temporal sequential projection images are discussed. The results are compared to other related methods. Moreover, the chapter provides an outlook to what should be addressed in future work.

Conclusions The last chapter intends to wrap up the thesis by summarizing it and stating the lessons learned.

2 Medical Background

This chapter provides an insight into medical aspects of the reconstruction problem. Relevant anatomical terms associated with the human rib cage are introduced, characteristics of the ribs in chest radiographs are described and background information on temporal subtraction techniques is provided. Afterwards, the resulting requirements for a rib cage reconstruction system are derived.

2.1 Anatomy and Functionality of the Rib Cage

The human rib cage (also referred to as bony thorax or thoracic cage) is a set of articulated bones, which is part of the skeletal system. It consists of various elements as the sternum, 12 thoracic vertebrae, 12 symmetrically arranged pairs of ribs, and costal cartilages.

Posteriorly (i.e., at the back of the body), there are 12 pairwise articulations of the ribs to the thoracic vertebrae. Vertebrae, which form the spinal column, are joined by intervertebral discs. The upper 10 pairs of ribs are additionally attached to the sternum at the anterior side (front) via flexible costal cartilages. The two lowest pairs of ribs are referred to as floating ribs, since they do not posses any fixation anteriorly. The ribs are separated by intercostal spaces. The sternum provides two attachment sides to the clavicles. Together with a pair of scapulae (one scapula attached to each clavicle) clavicles form the pectoral girdle (see Fig. 2.1).

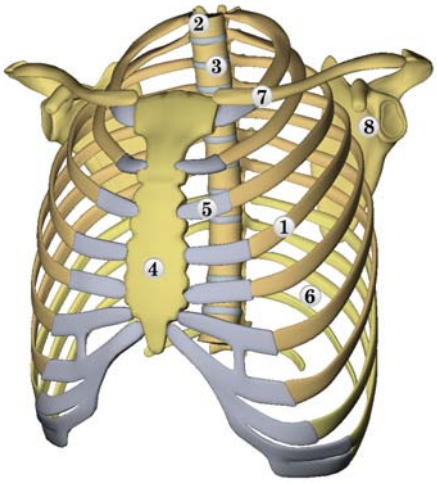

Figure 2.1: Schematic view of components of the rib cage: (1) rib, (2) vertebra, (3) intervertebral disc, (4) sternum, (5) costal cartilage, and (6) intercostal space. Clavicles (7) and scapulae (8) form the pectoral girdle.[1]

The rib cage's purpose is the protection of the vital structures of the thoracic cavity such as lungs, heart, liver and major blood vessels. It provides structural support for the pectoral girdle and upper extremities and serves the surrounding muscles as attachment site. Hence, the rib cage is an important component of the musculoskeletal system. Moreover, the rib cage supports the human respiratory system due to the special construction of the ribs with muscles between the intercostal spaces, which allow for costal breathing.

The bony structures of the thorax are suited to provide a reference system to define the pose of a patient, because bones vary marginally over time. However, since the

[1] The schematic view of the rib cage was obtained using BoneLab by Next Dimension Imaging: http://www.nextd.com/bonelab.asp

bones of rib cage and pectoral girdle are connected by multiple joints and flexible components, movements of individual structures are an issue: Clavicle and scapulae are coupled with the movement of the arms. Thus, their positions tend to vary considerably. The rib cage, on the other hand, is independent from this movement. Breathing, which is achieved by contraction and relaxation of intercostal muscles and the muscular diaphragm at the bottom of the thoracic cavity, causes the ribs to move [WRK+87]. Nevertheless, since the X-ray images are acquired at maximal lung capacity (for diagnostic reasons), the relative pose of the ribs should be closely the same in different images. Consequently, the ribs are an adequate choice to define a patient's pose.

2.2 Chest Radiography

Radiography is a projective imaging modality, which is attributed to the discovery of X-rays by Wilhelm Conrad Röntgen in 1895 [Rön95]. Even today, the technique, which revolutionized modern diagnostic medicine by allowing to study the interior anatomy in *living* subjects for the first time, plays a major role in differential diagnosis of the chest region.

Generating radiographs involves the projection of an anatomical 3D structures onto a 2D image plane. High energy ionizing radiation is emitted by an X-ray source, traversing the body. The ionizing radiation interacts with tissue in a way that energy is absorbed and the radiation is attenuated. The resulting differential attenuation is detected at the opposite side of the body to the radiation source. An X-ray image shows intensity values in each pixel that represent the attenuation of the X-rays, where the attenuation depends proportionally on thickness as well as on the density (and atomic weight) of the tissue traversed. The attenuation of the intensity of the incident radiation I_{in} emitted by the X-ray source to the transmitted

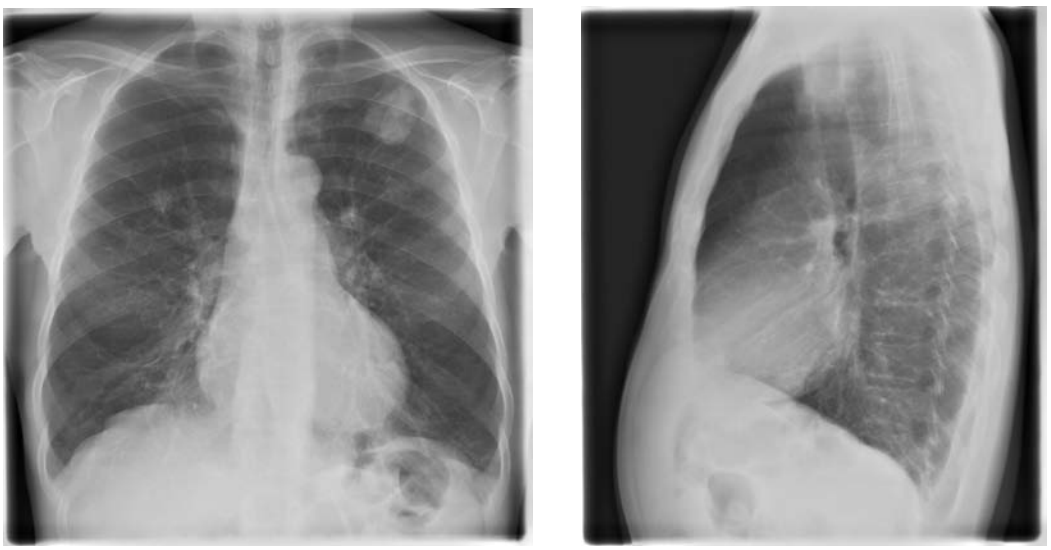

Figure 2.2: Standard posterior-anterior (PA) and lateral X-ray images: PA-radiographs are acquired with the radiation passing through the patient from the back to the front.

intensity I_{out} along a ray x can be expressed by the Beer-Lambert law

$$I_{out} = I_{in} \exp\left(-\int \mu(x)dx\right),$$

with $\mu(x)$, the linear attenuation coefficient,which varies for different types of tissue.

In clinical standard examinations, two radiographs, a posterior-anterior (PA) and lateral image, are acquired (see Fig. 2.2). In PA-images, the patient faces the detector such that the radiation passes the body from the back to the front. The patient is instructed to breath up to total lung capacity for the largest possible extension of the lungs to yield a maximal window to observe internal structures enclosed by the ribs.

It is important to be familiar with the characteristic appearance of the ribs within radiographs, since later, this will be a crucial factor for the choice of information used from the projection images for 3D reconstructions. Bones are composed of two different types of osseous tissue, cortical and spongious bone. In contrast to spongious bone, the highly calcified cortical bone possesses a very compact structure and is located on the bone's surface. This becomes apparent in radiographs, since the borders of ribs are contrasted against the background in those regions where the radiation penetrates the bone surface in tangential direction (see Fig. 2.3).

Another characteristic of ribs in radiographs is that the contrast between ribs and surrounding tissue qualitatively differs in PA and lateral images. Due to a higher degree of superposition by other thoracic structures, identifying the ribs in the lateral view is more difficult than in PA-views. In lateral images, it is also very difficult to distinguish between ribs that are located on the right body side and those on the left. More information on the matter of radiologic appearance of ribs in chest radiographs as well as on counting and identification of individual ribs (especially in lateral views) can be found in the article of Kurihara et al. [KYM+99].

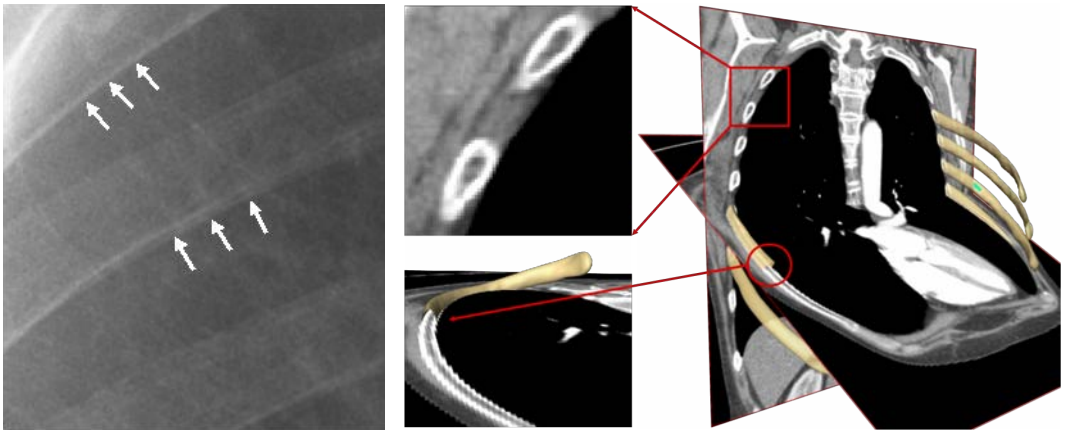

(a) (b)

Figure 2.3: The appearance of cortical bone in radiographs: (a) The border of ribs appears reasonably contrasted within radiographs due to material properties of the compact cortical bone layer on the rib's surface. (b) The CT-image of the chest clearly indicates the calcified layer of compact cortical bone (white).

2.3 Image Subtraction in CAD

The following section provides an overview of image subtraction techniques with application to (chest) radiographs for diagnostic purposes.

Image subtraction allows for the detection of differences between two images. An informal and simple illustration of the way image subtraction works is given in Fig. 2.4. The principle of image subtraction is widely used in computer-aided diag-

(a) (b) (c)

Figure 2.4: Images subtraction works like the well-known children's game "spot the difference" between two images in (a) and (b). The differences, which are only detectable on a closer inspection, become clearly visible in the subtraction image (c).[2]

nosis (CAD) to enhance anatomical structure or findings of interest and to suppress irrelevant and distracting structures. There are various fields of applications, as for instance, in dentistry for the diagnosis of caries and periodontal defects [HSK08], or in the detection of vascular disorders, where digital subtraction angiography is used for the visualization of blood vessels [MNV99].

If a subtraction is obtained from two images, which were acquired at different times to detect a change over a time interval, then the image subtraction is referred to as *temporal* subtraction. Temporal subtraction is especially suited to identify subtle changes. In comparison to conventional diagnosis using radiographs, the detection of diseases in early stages is possible and the performance of radiologist can be improved [KKH+06, DMX+97]. One common application of temporal subtraction is the diagnosis of pulmonary diseases using chest radiographs [JKT+02, TJK+02, LMVS03].

As stated before, a major problem in generating adequate temporal subtraction is the difference in the patient's pose during the image acquisitions of two radiographs. To compensate for this 3D difference, deformable 2D registration approaches are commonly used, which align corresponding structures in the two radiographs. However, due the projective nature of the images with superposition of multiple structures, finding unique correspondences between the image may not be possible (see Fig. 2.5). Consequently, it is likely that there is no unique solution to the 2D image registration problem, which provides an equally perfect alignment of all the structures in the images.

This work is motivated by supporting and improving temporal image subtraction of chest radiographs. Fig. 2.6 illustrates that the 3D information on 3D pose differences obtained with methods devised in this thesis shall be used besides the available

[2] The cartoon is taken from "Find Six Differences" by Bob Weber, http://www.kidcartoonists.com/wp-content/uploads/2007/07/six-diff.jpg.

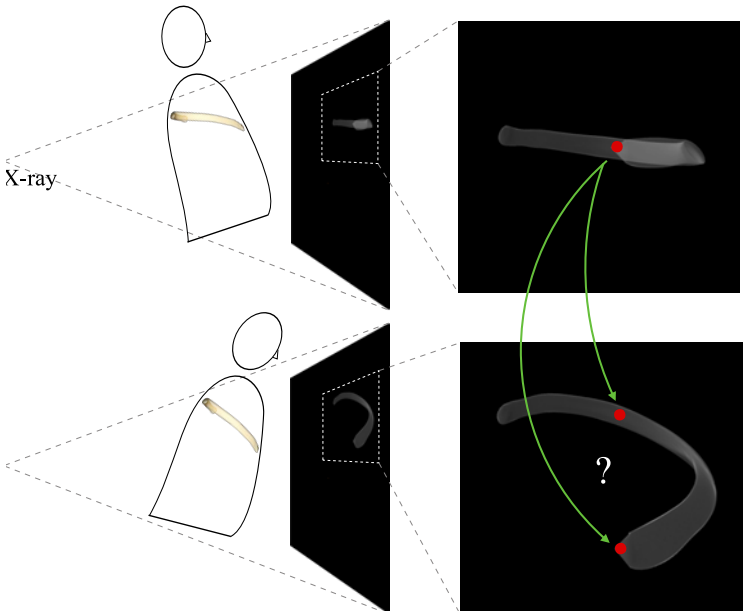

Figure 2.5: Solving the 2D registration problem for aligning corresponding structures in two radiographs, which exhibit a difference in the patient's 3D pose, is challenging. The schematic view illustrates two projection images of a single rib. Due to a PA-inclination of the patient it is impossible to define corresponding points between the projection images.

2D information in the radiographs.

2.4 Requirements and Challenges

In this section, requirements for a rib cage reconstruction system are derived.

Automation The 3D reconstruction of the pose and shape of the rib cage from projection images is a very complex task, since it involves the simultaneous estimation of various properties (the orientation, position, size, and shape) from very limited data. For instance, a segmentation (i.e., the delineation of structures from the surrounding background in, for example, radiographs or tomographic data) can be performed manually, although this task is extremely time consuming. Obtaining a 2D/3D reconstruction manually, on the other hand, is simply not feasible, which makes the automation of the task obligatory. Thus, the goal is of this work is to devise methods that can handle 3D reconstructions automatically.

Data Input A reconstruction from radiographs, in comparison to tomographic data, is advantageous, since the patient is exposed to a lower dose of radiation and health care costs are reduced. These benefits come at expense of limited information, which is available for a reconstruction.

There are two counteractive requirements regarding the number of projection images used. From an algorithmic point of view, the use of multiple 2D images (> 2), which are acquired from different directions, can increase the information at hand. From a clinical point of view, however, it is necessary to use as few radiographs as possible. Thus, a trade-off needs to be considered between feasibility and applicability in a clinical context. While in clinical practice two radiographs (one posterior-anterior (PA) view and one lateral view) are acquired in most examinations, there

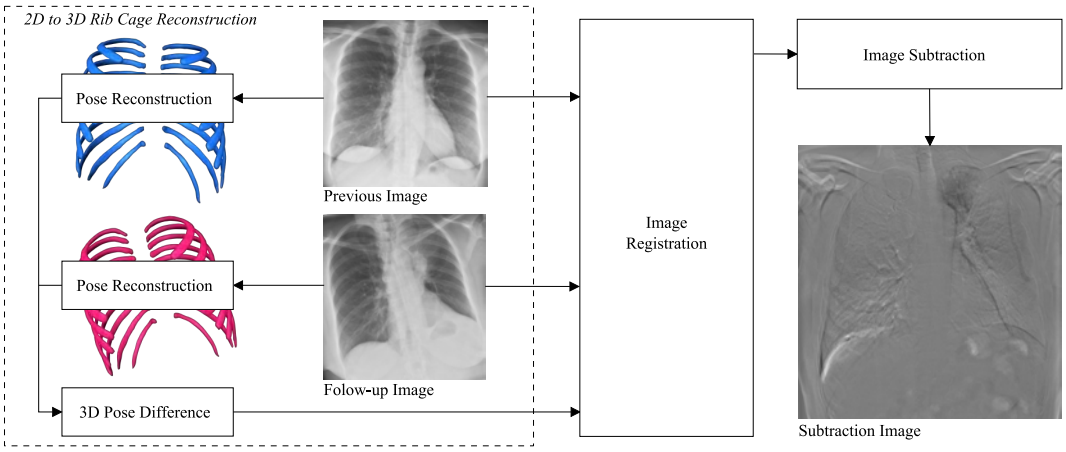

Figure 2.6: Overview of the CAD-system for temporal image subtraction.

is no standardized imaging protocol for their acquisition. The patient commonly turns approximately 90° for the lateral view. Consequently, PA and lateral X-ray images do not depict the same scene. This makes the problem of the 3D shape and pose reconstruction from two views more difficult. Although there are special X-ray imaging devices that can be configured to generate a calibrated, biplanar pair of radiographs (PA and lateral), as described in [DCD+05] and used in [BLP+08], they are not widely used yet. In addition, identifying the ribs in the lateral view is more difficult due to a higher degree of superposition by other thoracic structures. For the above reasons the 3D shape as well as pose reconstruction of a patient's individual rib cage should be preferably accomplished from one PA-projection.

Left with such reduced information, it is indispensable to incorporate a-priori knowledge into the reconstruction process. Part of the idea is to start with an initial estimate of the solution. More precisely, a 3D template of a rib cage's shape is used and adapted to the radiographs. The adaption of the 3D template is constrainted, as it can only be modified in a such a way that it maintains a shape that is typical for a rib cage. For this reason, this reconstruction approach is based on a statistical shape model of the rib cage, which exhibits the described property.

Another difficulty involved in a 3D reconstruction from X-ray images is that the reconstruction process relies on the detection of features that represent the anatomy in the X-ray images. In this work, it is assumed that the ribs can be segmented from X-ray images. In most situations this assumption is met, since rib boundaries can be, at least, outlined manually. The automated extraction of rib contours is a challenging problem, which is still an open research problem and does not lie within the scope of this work. However, the prospect of solving this problem is important and given, since various promising approaches for the segmentation of the ribs in radiographs have been proposed. For instance, work to extract the contours of posterior ribs from frontal X-ray images has been reported [vGtHR00, YGA95, LvG06]. Plourde et al. [PCD06] achieve a semi-automatic segmentation of both posterior and anterior parts of the ribs. Furthermore, Park et al. address the problem of detecting and labeling the ribs [PJW03].

3 Related Work

Existing work is introduced that addresses the problem of reconstructing 3D information from 2D projections. At first, methods are presented that are specifically related to the application of reconstructing the 3D shape of the rib cage from X-ray images. Second, related work is introduced that addresses the problem of *model-based* reconstruction of 3D geometries from 2D projections in general. The methods are classified according to those that primarily deal with (a) pose or (b) shape reconstruction. Afterwards, common distance measures are presented and 2D to 3D reconstruction methods are compared according to their approach to build correspondences between a 3D model and 2D images.

3.1 Reconstruction of the Rib Cage from X-ray Images

One of the first methods for the reconstruction of the human rib cage was proposed by Dansereau and Srokest [DS88] to assess geometric properties of the rib cage of living subjects. It uses direct linear transformation (DLT) [Mar76] for the reconstruction of manually extracted rib midlines from a pair of stereo-radiographs (one conventional PA-view and a second PA-view with 20° difference of the X-ray source's incidence angle, see Fig. 3.1).

Delorme et al. [DPdG+03] presented an approach to generate patient-specific 3D models of scoliotic spines, pelvises and rib cages. They used the method of Dansereau and Srokest [DS88] in combination with an additional lateral view (cf. Fig. 3.1) to obtain 3D coordinates of anatomical landmarks that need to be manually identified in the 2D radiographs. A generic 3D model of a scoliotic patient, reconstructed from computer tomography (CT), is adapted to these landmarks using free form-deformation to estimate patient-specific surface models.

The work of Novosad et al. [NCPL04] addresses the problem of estimating the pose of vertebrae to reconstruct the spinal column for the analysis of the spine's flexibility. This work is similar to ours in that patient-specific 3D shape reconstructions from projection images are used to perform a subsequent pose reconstruction. For the prior 3D shape reconstruction, Novosad et al. adapted the method described by Delorme et al. [DPdG+03]. The pose is then reconstructed using only one PA X-ray image.

Recently, two works using a semi-automated framework for the reconstruction of the rib midlines have been presented by Mitton et al. [MZB+08] and Bertrand et al. [BLP+08]. Their approaches depend on a prior 3D reconstruction of the spinal column and two calibrated, exactly perpendicular, and simultaneously acquired radiographs (PA and lateral) [DCD+05]. A generic model, fitted to previously reconstructed landmarks of the sternum and entry points of the ribs at each vertebra (using the same technique as in [DPdG+03]), yields an initial estimate for the reconstruction. This estimate is iteratively improved with the interaction of an operator

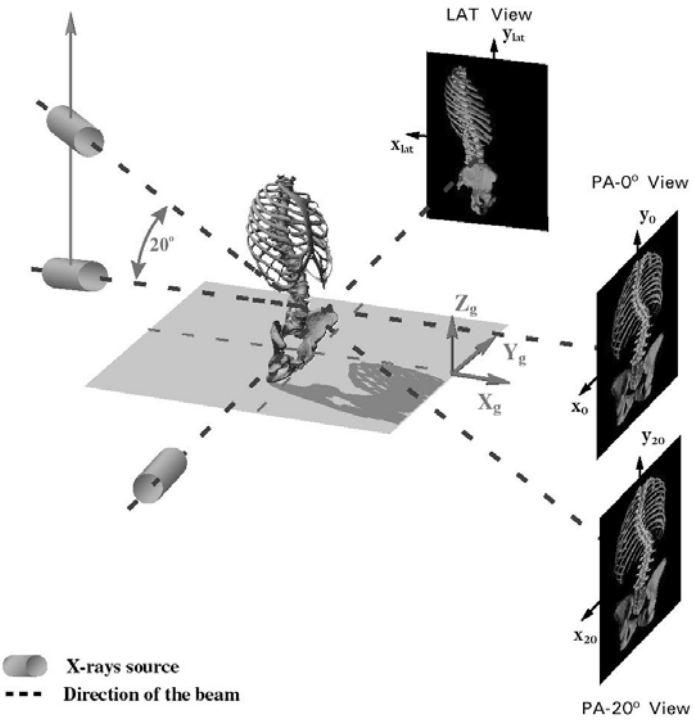

Figure 3.1: Geometric image acquisition setup for stereo-radiographs: Dansereau and Srokest [DS88] perform a reconstruction from one standard PA-view and a second PA-view, which is aquired with an X-ray source angled down 20°. Delorme et al. use an additional lateral view (adopted from [DPdG+03]).

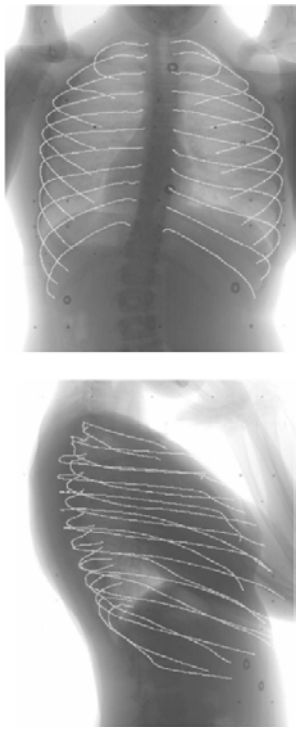

Figure 3.2: Benameur et al. recover the midlines of ribs from standard PA and lateral X-ray images (adopted from [BMDDG05]).

who manually adapts projected rib midlines of the generic model to image information in the radiographs.

These rib cage reconstruction methods [BLP+08, DS88, DPdG+03, MZB+08] depend on the identification of landmarks within the X-ray images. The correct identification of anatomically relevant landmarks of the ribs in X-ray images is difficult even when performed manually. A promising alternative is the use of features from X-ray images that are more likely to be detected automatically, e.g., rib contours or image gradients. Moreover, the methods do not take advantage of a-priori knowledge about the rib cage's shape variability due to the use of the DLT technique. Benameur et al. [BMDDG05] approach this problem using 3D SSMs of rib midlines and extracted contours from a calibrated pair of X-ray images (PA and lateral view). The reconstruction is obtained by minimizing an energy function defined via edge potential fields between rib contours and projected rib midlines (cf. Fig. 3.2) of an SSM. This method is used to classify pathological deformities of the spinal column in scoliotic patients.

The recent work of Koehler et al. [KWG09] proposes a template-based approach to approximate the 3D shape of the ribs from two segmented radiographs (PA and lateral view). A segmentation of individual ribs, obtained with the method of Plourde et al. [PCD06], is classified according to whether it belongs to the anterior, lateral, or posterior part of a rib. Based on this classification, the vertices of a 3D rib template model are annotated. Then, each rib is reconstructed individually by aligning the corresponding parts to the segmented X-ray image (see Fig. 3.3). The alignment to the PA-view is subsequently improved by adapting the template to the outer border of the rib cage in the lateral view. So far no quantitative validation of the method is available. Furthermore, no reliable ground truth was used to assess the reconstruction accuracy, as the reconstruction quality is measured by comparing the area overlap between the segmentation of the PA-view and the projection of the reconstructed 3D model. However, our experiments (cf. Sect. 6.2.5 and Fig. 6.8) indicate that the relation between the model's matching quality to one PA-view and the actual reconstruction result is highly ambiguous and, hence, is no adequate basis for a validation.

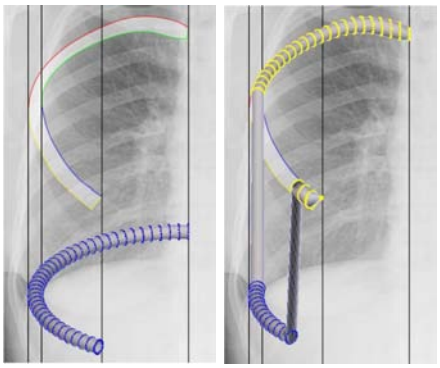

Figure 3.3: Template fitting according to Koehler et al: Based on a classification of anterior, lateral and posterior parts of the ribs in a segmented PA view, vertex clusters of a template assigned to one of the three parts are fitted to the image data (adopted from [KWG09]).

The method presented in this thesis is similar to the work of Benameur et al. [BMDDG05], as it uses a 3D SSM and relies on edge-based features in the image data, instead of landmarks that have little prospect of being detected automatically from radiographs. However, in contrast to [BMDDG05], we use an SSM of the rib's *surfaces*. The approach, that is proposed in this thesis, allows for a direct comparison of rib contours in both, the model projection and the image data, where Benameur et al. propose to compare projected midlines of the model with contours of the ribs in the image data. Furthermore, in [BMDDG05] 3D reconstructions obtained with the method of Dansereau and Srokest [DS88] are used as gold standard to evaluate the method, which limits the assessment of the method's accuracy. We use 3D surface models of rib cages, extracted from CT-data of 29 different subjects, as reliable gold standard in our evaluation.

3.2 2D/3D Reconstruction

In this section, methods for the 3D reconstruction from 2D images are presented that follow a similar model-based approach as the method presented in this thesis. Work that primarily addresses the problem of the reconstruction of the pose *or* the shape is examined. Most of the described methods are based on the iterative closest point (ICP) algorithm [BM92], a general method for aligning shapes by generating pairs of corresponding points between two shapes to be matched. The ICP algorithm and

the task of establishing point correspondences between 3D model and 2D images is examined in the Sect. 3.3.3.

Note that the methods, which will be introduced in the following two sections, deal with the femur [FL99, Zhe06, BLH07, MBF+06], the pelvis [LWH06] and individual vertebrae [LS95, CKSK00]. Thus, they address only *single* bones. The reconstruction of *bone ensembles* with repetitive structures as the rib cage and the spine is considered much more challenging, because similarity and redundancy of sub-structures can lead to mismatches. Hence, those existing methods can not be applied to our reconstruction problem without suitable modifications.

3.2.1 Pose Reconstruction

In recent years, several methods for the pose reconstruction of 3D objects from 2D projection images were introduced [FAB95, LS95, CKSK00, BLH07]. The work of Lavallée and Szeliski [LS95] deals with determining the position and orientation of a given surface of arbitrary shape, based on contour points in 2D image data. The matching is achieved by minimizing signed distances from the 3D surface to projection lines, i.e., lines defined between 2D contour points and the projection center. A similar approach to [LS95], which uses an extended ICP method, was introduced by Feldmar et al. [FAB95]. Instead of using signed distances the approach exploits surface normals.

Since ICP-based methods strongly depend on the initialization and may lead to local optimal solutions, Cyr et al. [CKSK00] suggested a hierarchical iterative matching approach to avoid this problem. Here, the projection direction of vertebrae is recovered from one binary projection image without considering the translation of the object with respect to the location of the projection source.

Yamazaki et al. [YWN+04] proposed a reconstruction approach to estimate the 3D pose of knee implants from single 2D fluoroscopic images. Their objective is to enable *in-vivo* motion analysis of implants (in living patients) to improve treatment in total knee arthroplasty. While their approach is based on an adapted version of Lavallée's and Szeliski's method, Yamazaki's work focuses on an improved depth positioning, i.e., the correct estimation of the translation in the direction of projection, which is especially hard to achieve from a single projection image. The authors propose a global optimization approach to determine the depth position.

An approach that is also motivated by motion analysis of implants performs 3D pose estimations from a calibrated stereo-pair of radiographs. The method, which was presented by Bruin et al. [DBKS+08], does not rely on the adaptation of a 3D surface to the radiographs, but on the 2D/3D registration of 3D CT-data. The pose of the CT-data is iteratively adjusted such that digitally reconstructed radiographs (DRR, see Sect. 3.3.1) generated from the CT-data and the stereo-radiographs are matched. The application of analyzing motions of implants is similar to our problem because differences in the pose between subsequent radiographs are determined to detect a possible loosening of an implant over time.

The aforementioned methods address the problem of recovering the pose of *known* shapes from their projections. With regard to medical applications, however, it is often required to assess the pose of an *unknown* patient-specific shape of a known anatomical class. The method presented by Bhunre et al. [BLH07] accomplishes this

for the proximal and distal femur by fitting a generic model to one patient-specific X-ray image. For complex geometries, as the rib cage, this approach is not likely to yield accurate results, because such structures are often subject to a high inter-patient variability and involve symmetry or even repetitive structures as the ribs. For this reason, it is also necessary to retrieve the specific 3D shape of a patient's anatomy to estimate its pose from projection images correctly.

3.2.2 Shape Reconstruction

Several shape reconstruction methods have been proposed that use a-priori knowledge [FL99, LWH06, Zhe06, BMDDG05, MBF+06], e.g., in form of statistical shape models (SSMs). An SSM [CTCG95] is a deformable model that is derived from a set of training shapes. It incorporates information about reasonable variations in a class of shapes. SSMs will be introduced in more detail in Sect. 4.3.

Fleute and Lavallée [FL99] retrieve the shape of the femur from segmented contours in X-ray images with an SSM. They use a generalized version of the ICP algorithm to minimize the distance between apparent contours on the SSM's surface and a set of projection lines as already used in [LS95]. Apparent contours are 3D contours along those points on the SSM's surface at which the X-rays' angle of incidence is tangent to the surface.

The shape reconstruction method presented by Lamecker et al. [LWH06] estimates the shape of the pelvic bone from few projection images. It is motivated by computer-aided preoperative planning for the treatment of degenerative joint diseases. The reconstruction of the 3D shape of a patients's pelvis is intended for biomechanical simulations to predict postoperative loads and forces between pelvis and joint implant. The method also uses an SSM, which is adapted to the 2D projection images. In contrast to the work of Fleute and Lavallée [FL99], the adaption is achieved by the minimization of a distance measure between the 2D images and projections of the SSM (*thickness images*), based on the *silhouettes* in both images. Thickness images are computed as perspective projections from the lengths of rays propagated through the enclosing surface volume of the SSM (see Fig 3.4). The pose of the shape to be reconstructed is assumed to be known in advance.

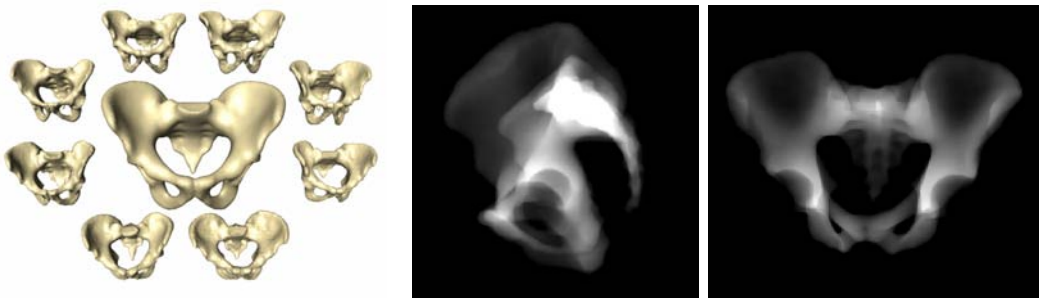

(a) (b)

Figure 3.4: Shape reconstruction of the pelvis according to Lamecker et al.: (a) the trainings set and the mean model (center) of a statistical shape model and (b) thickness images of the SSM (adopted from [LWH06]).

3.3 Distance Measures

Matching objects is a fundamental problem that arises in various fields of applications in computer vision and medical image analysis. Metrics to measure the similarity between objects to be matched are required. A common approach is to use distance measures, which, in case of medical image data, often rely on information of the patient's anatomy within the images. The majority of these measures can be classified into techniques that are either based on geometrical features like edges and regions (*feature-based*) or on intensity values in images (*intensity-based*) to quantify the similarity.

3.3.1 Intensity-based Methods

Intensity-based distance measures operate on the entire image by computing statistics on the intensity values contained in each pixel (or voxel) of the two images to be matched. In most approaches, the images are required to be of the same dimensionality. Considering the problem to adapt a 3D object to a 2D projection, the 3D object needs to be transformed (i.e., projected). Thus, the 3D object, encoding details as for example tissue density, is projected via a suitable projection algorithm.

In the work of Yao [Yao02] and Taylor [YT00] a statistical atlas is generated from segmented CT-data using a tetrahedral mesh representation. Besides shape properties, such a model contains information about the bone density in terms of density distribution functions in each tetrahedron of the mesh. The mesh can be used to generate simulated X-ray images by modeling the attenuation of X-rays through the tetrahedral volume using a projection algorithm. The simulated X-ray images can then be compared to the real X-ray images on the basis of the intensity values in both images to obtain a 3D reconstruction. Sadowsky et al. [SCT06] propose such an projection algorithm based on a technique to simulate X-ray projections from volumetric intensity data, that is known as digitally reconstructed radiography (DRR). DRR's are generated by sending rays through a volume and integrating the attenuation information (commonly represented by Hounsfield units) along each ray. DRR is also widely used in the field of multimodal 3D/2D registration to generate simulated radiographs from CT-data with the goal to align the CT-volume to patient's X-ray images [DBKS+08].

There are various distance measures to compare intensities in images. Among them are mutual information, cross correlation, entropy of difference images, pattern intensity, and gradient difference to name a few. For a more detailed description of the different measures and a comparative evaluation regarding the matching of 3D objects to 2D images, refer to the work of Penney et al. [PWL+98] and Steininger et al. [SFK+08].

The benefit of intensity-based distance measures is that they do not require preprocessing to extract features from the images. Thus, their performance is not biased by an error-prone feature extraction. Without filtering the images, however, the matching algorithm is sensitive to additional structures that are not contained in both images that are to be compared.

3.3.2 Feature-based Methods

Feature-based techniques require the identification of sets of ideally corresponding, geometrical features in both of the objects to be aligned. These features can be anatomical landmarks, which are salient points of distinct anatomical meaning in both images. Landmarks have been used for the reconstruction of the rib cage in [DPdG+03, NCPL04, DCD+05]. In projection images, it is difficult to accurately locate them, even with user interaction.

Another approach is to use extracted edges or entire contours of anatomical structures. This has been used for aligning 3D models represented by surfaces (e.g. extracted from CT data or in form of an SSM) to contours in 2D images in [LS95, FAB95, BLH07, YWN+04] and [FL99, LWH06, Zhe06]. The efficient computation of edge-based distance measures, as used in this work, has been investigated in the past. For instance edge-based template matching using the Hausdorff distance was applied to quickly locate objects within images [Ruc97, DJ94]. The Hausdorff distance penalizes high local deviations between two contours. Depending on the application, other distances, as the Euclidean or the Mahalanobis distance may be more suitable.

Besides distances between edges or points, there are other geometrical features like normals and curvature of contours or surfaces to locally measure similarity. Furthermore, the overlap of regions or the comparison of areas are utilized.

Although feature-based distance measures rely on a pre-processing step to extract features, the performance benefits from the reduction in the number of data points to be analyzed.

3.3.3 Building Correspondences

Since the reconstruction method proposed in this work is based on building point correspondences via a distance measure, a review of existing approaches to set up correspondences in 2D/3D reconstruction problems is given.

A general and widely used method for the rigid alignment of shapes is the iterative closest point (ICP) algorithm [BM92]. Starting with an initial transformation estimate of the shape to be matched to a reference shape, pairs of corresponding points are generated between the two shapes. Then, the initial transformation and the point correspondences are iteratively adjusted, such that an error metric is minimized. The general method of ICP is outlined in Algorithm 1.
The algorithm terminates in case the mean squared distance error e falls below a defined threshold

$$\epsilon > |e^{(k)} - e^{(k+1)}|, \tag{3.1}$$

or if the current transformation reveals no significant change compared to the previous iteration,

$$\tau > |T^{(k)} - T^{(k+1)}|. \tag{3.2}$$

Alternatively, a maximal number of iterations can be defined.

ICP converges monotonically and relatively quickly to a close local minimum. Thus, the outcome of the alignment highly depends on the initial transformation $T^{(0)}$. Due to the way ICP determines correspondences, the relation, set up between the two shapes $P = \{\mathbf{p}_i\}$ and $Q = \{\mathbf{q}_j\}$, may not be bijective (one-to-one). This

Algorithm 1: Iterative Closest Point

Input: two shapes represented as point sets $P = \{\mathbf{p}_i\}(i = 1, ..., n)$ and $Q = \{\mathbf{q}_j\}(j = 1, ..., m)$; initial rigid transformation $T^{(0)}$

Output: rigid transformation $T^{(k)}$ that aligns P with Q

```
k ⟵ 0
repeat
    foreach p_i^(k) do
        compute the closest point c_i^(k) such that d(p_i, Q) = min_{c_i ∈ Q}(||p_i − c_i||)
    end
    determine T^(k) such that e^(k) = (1/n) Σ_{i=1}^{n} ||T^(k)(p_i^(k)) − c_i^(k)||^2 is minimized
    P^(k+1) ⟵ T^(k)(P)
    k ⟵ k + 1
until termination criteria reached
```

means that the function $c : P \rightarrow Q$ is not necessarily injective and surjective, since two points p_i can be mapped to the same q_j; and a point q_j may not be assigned to any p_i. As a consequence, the desired solution may not be found.

There are many different variants of the ICP method. A comparison of ICP variants can be found in [RL01].

Most of the model-based methods described in Sect. 3.2 are related to the ICP method. The authors have adapted and extended ICP in different directions. The methods provide possibilities to find more meaningful and suitable correspondences and differ in the way the transformation $T^{(k)}$ is determined and the error metric is minimized. More importantly for the 2D/3D reconstruction problem, these methods introduce ways to establish point correspondences between shapes in different dimensions (i.e., a 3D model and 2D projection images). Where the original ICP is restricted to determine a rigid transformation only, the adapted methods enable the estimation of additional parameters that control the size and shape of the object to be matched. Methods, that rely on point correspondences, can be distinguished in their approach to generate correspondences between the 3D model and the projection images.

Lavallée et al. [LS95] and Fleute et al. [FL99] set up 2D/3D correspondences between contour points in the 2D image and a 3D surface directly [LS95] or the apparent contour points of the surface [FL99]. The corresponding points are determined by the shortest distance between the surface points and the projection rays.

An alternative approach, proposed by Laporte et al. [LSDG+03] and used by others [MZB+08, BLP+08], is the *non-stereo corresponding contour* (NSCC) method. The algorithm identifies 2D contours in form of a point set I in the radiographs. Apparent contours of the generic, static 3D model A_{3D} are extracted and projected to form an associated set of 2D contour points P, where each point in P corresponds to a point in A_{3D}. In a next step, correspondences are set up between the two 2D contours I and P based on a point-to-point distance. The correspondences are iteratively refined and used to estimate a rigid transformation as well as a deformation

of the 3D model in an ICP-like manner.

Zheng et al. [ZGS+09] first, establish point correspondences between contours in the 2D image I and contours from the projection of a 3D surface model A using a *symmetric injective nearest-neighbor* (SIN) mapping operator. The SIN mapping ensures that (1) each point in both contours is only mapped to at most one point on the other contour, (2) these matched pairs of points are symmetrically closest points, and (3) no cross-matching occur, as illustrated Fig. 3.6(top). The 2D point correspondences are then used to build 3D to 3D correspondences between the 3D model and back-projected 2D contour points of the 2D image (see Fig. 3.5). The reconstruction is accomplished using the 3D to 3D correspondences.

Delorme et al. [DPdG+03] establish 3D to 3D point correspondences between anatomical landmarks. For this, 3D points are reconstructed from landmarks in the 2D images using DLT. A 3D model, with landmarks that correspond to the reconstructed 3D point, is deformed using a 3D geometrical free-form deformation to match the 3D points.

In the work of Lamecker et al. [LWH06], 2D to 2D correspondences from contours of the projection of an 3D SSM and contours within the 2D image (and vices versa) are determined via the computation of the two-sided Euclidean distance between the points of both contour sets. No explicit correspondences between the 3D model and the 2D image need to be used.

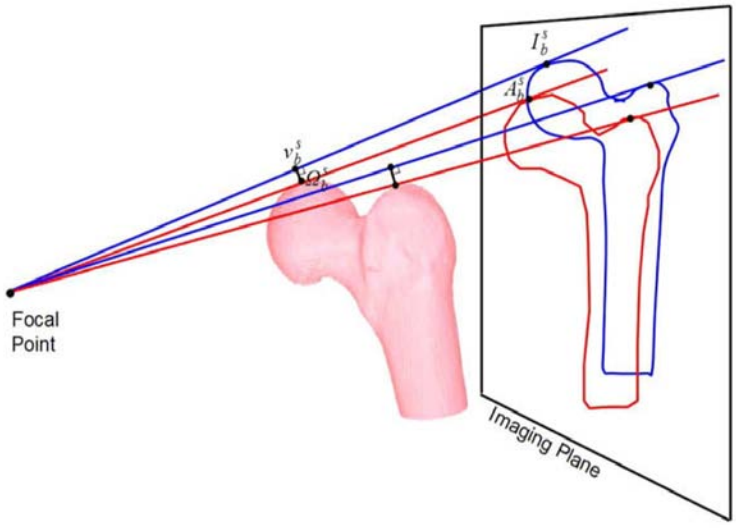

Figure 3.5: Correspondence building according to Zhang et al.: For points of the image contour I, associated 3D points $\mathbf{v}$ are determined, which are located on the projection line between the focal point of the projection source and the points in I. The points in $\mathbf{v}$ possess the shortest distance to the apparent contour Ω of the 3D surface (adopted from [ZGS+09]).

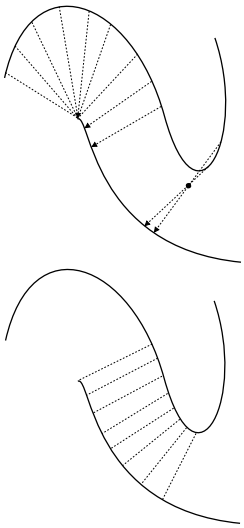

Figure 3.6: Point correspondences build using ICP (top) in comparison to the SIN mapping operator of Zhang et al. (bottom).

4 SSM-based Geometry Reconstruction from 2D Projection Images

This chapter describes the general reconstruction method used, independently from the object or anatomy we wish to reconstruct. It presents the components of the SSM-based reconstruction approach. This includes an introduction to statistical shape models (SSMs) to provide a fundamental understanding of how variations that are typical for a type of object can be modeled. Furthermore, the basics of projections of 3D objects to the 2D image space are described, which will be applied to generate projections of the SSM. Afterwards, details on the optimization process are given.

4.1 Reconstruction Process

Below, we describe the essential components of the SSM-based reconstruction method and their interaction.

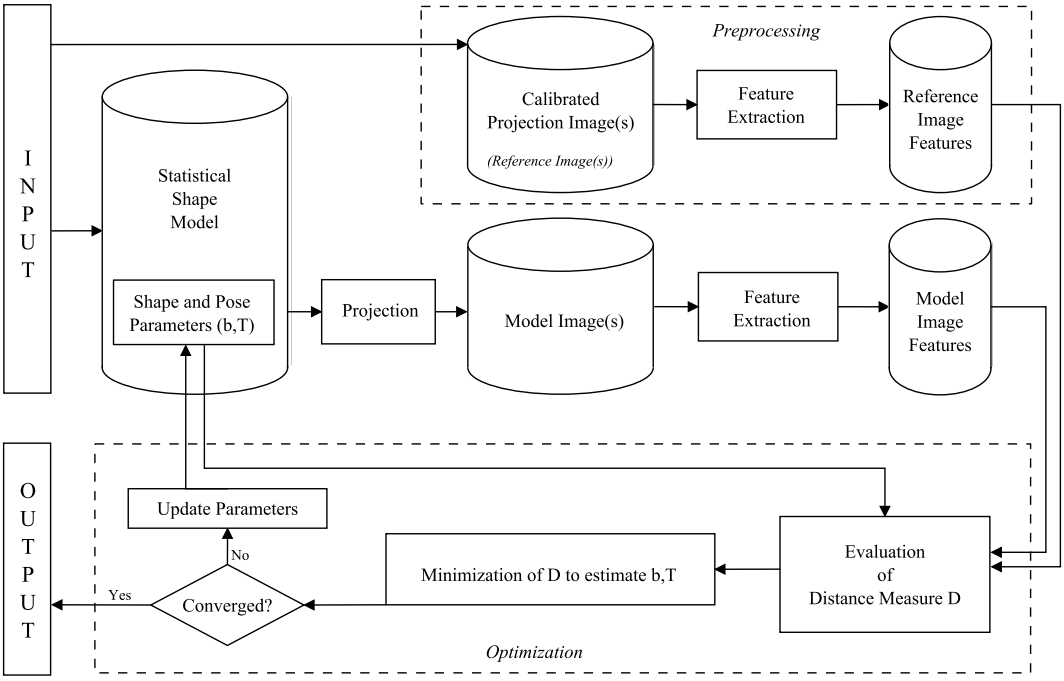

Figure 4.1: Scheme of the SSM-based reconstruction process (refer to Sect. 4.1 for a detailed description).

The goal of this work is to solve two problems: (1) The 3D shape reconstruction of an individual shape belonging to a specific class and (2) its 3D pose reconstruction, each from few 2D projection images. For a shape reconstruction, not only the 3D shape, but also the 3D position, orientation, and size must be determined. For the pose reconstruction only the latter parameters (3D position, orientation, and size) are recovered.

The aim of the reconstruction process is to infer these parameters from the projection data. The idea is to obtain a 3D model that serves as an estimate for the 3D pose (and 3D shape) of the individual rib cage. For this purpose, a parameterized 3D model S is fitted to the 2D projection images (*reference images*). In case of the 3D shape reconstruction, this model is an SSM, which is deformable and has been derived from a set of training data (see Sect. 4.3). The SSM is denoted as $S(\mathbf{b}, T)$, where T and $\mathbf{b}$ control the SSM's pose and shape, respectively. For a pose reconstruction, we use a patient-specific, non-deformable model. Thus, the shape of the patient's anatomy is known in advance and does not need to be determined. Fitting an SSM to the image data is accomplished in several steps, which are structurally illustrated in Fig. 4.1 and procedurally summarized in Algorithm 2.

Algorithm 2: SSM-based Reconstruction Process.

Input: reference images $I_r^{(i)} \in \mathbb{R}^2$; statistical shape model S with initial shape and pose parameter $(T^{(0)}, \mathbf{b}^{(0)})$; number of reference images n
Output: optimal $S(\mathbf{b}^*, T^*)$

for $i = 1, \ldots, n$ **do**
  $\mathbf{f}_r^{(i)} \longleftarrow$ feature extraction from $I_r^{(i)}$
end
$j \longleftarrow 0$
repeat
  $v^{(j)} = 0$
  for $i = 1, \ldots, n$ **do**
    $I_m^{(i)} \longleftarrow P^{(i)}(S(\mathbf{b}^{(j)}, T^{(j)}))$
    $\mathbf{f}_m^{(i)} \longleftarrow$ feature extraction from $I_m^{(i)}$
    $v^{(j)} \longleftarrow v^{(j)} + D(\mathbf{b}^{(j)}, T^{(j)})$
  end
  determine new parameters $(\mathbf{b}^{(j+1)}, T^{(j+1)})$, for which $v^{(j+1)} < v^{(j)}$
  $j \longleftarrow j + 1$
until *termination criterion reached*

In a preprocessing step, image features $\mathbf{f}_r$ (e.g. contours) are extracted from a set of n reference images $I_r^{(i)} (i = 1, ..., n)$. The SSM's parameters $\mathbf{b}$ and T, which control its shape and pose, respectively, are initialized with respect to a virtual image acquisition setup that corresponds to the acquisition setup of the reference images. During the iterative reconstruction process, the 3D SSM is projected ($P(S(\mathbf{b}, T))$) to obtain model images ($I_m^{(i)}$) in each iteration j. Image features $\mathbf{f}_m^{(i)}$ are extracted from the model image as well. On the basis of a distance measure D and the image features $\mathbf{f}_m^{(i)}$ and $\mathbf{f}_r^{(i)}$, the dissimilarity between model and reference images

is quantitatively measured ($v^{(j)}$). The dissimilarities are iteratively reduced by an optimization process that minimizes v and thereby adapts the parameters $\mathbf{b}$ and T until a termination criterion is reached.

A pose reconstruction using a patient-specific rib cage model proceeds analogously, except that no shape parameters need to be estimated. (See Sect. 4.4 for the generation of model images, Sect. 4.5 for details on the optimization, and Sect. 5.2 for the definition of distance measures.)

4.2 Preliminaries

This section defines concepts, which are used throughout the following chapters.

Definition (Image)**.** *A continuous mapping $I : D_c \to R_g$ with a domain $D_c \subset \mathbb{R}^2$, representing a space of spatial coordinates, and a range $R_g \subset \mathbb{R}$ of gray values g, representing intensity information within a gray level interval $[l_{min}, l_{max}]$ with $l_{min} \leq g \leq l_{max}$, is called image.*

Definition (Binary Image)**.** *An image $I_b : D \to \{0, 1\}$ with a range restricted to $\{0, 1\}$ is a binary image.*

Definition (Triangulated Surface)**.** *A compact, piecewise linear surface, which consists of finite sets of simplices (vertices V, edges E, and triangular faces F) whose connectivity is defined by a simplicial complex K, is referred to as triangle mesh or triangulated surface. The surface is geometrically embedded in $\mathbb{R}^3$, where the positions of the vertices in V specify the shape of the surface.*

Definition (Linear Transformation)**.** *Let $T : \mathbb{R}^3 \to \mathbb{R}^3$ be a geometrical transformation that maps $\mathbf{x} \in \mathbb{R}^3$ and $\mathbf{x}' \in \mathbb{R}^3$ such that $T(\mathbf{x}) = \mathbf{x}'$. T is called a linear transformation, if $T(\mathbf{x} + \mathbf{y}) = T(\mathbf{x}) + T(\mathbf{y})$ and $T(\alpha\mathbf{x}) = \alpha T(\mathbf{x})$ is satisfied, where $\mathbf{y} \in \mathbb{R}^3$ and $\alpha \in \mathbb{R}$.*

There are different types of linear transformations. A *rigid transformation* denotes a rotation and translation. *Similarity transformations* extend rigid transformations by uniform scaling, whereas *affine transformations* allow for translation, rotation, anisotropic scaling, and shearing.

4.2.1 Transformation Parameterization

The problem of a 3D pose reconstruction is to find a geometric transformation T of a 3D model that specifies the orientation, position (rigid transformation) and optionally the scale (similarity transformation) of the examined anatomy at the time the reference images were obtained. T is represented by a set of parameters, which are determined via an iterative optimization procedure (see Sect. 4.5). To provide a solid basis for the optimization, the search space needs to be parameterized carefully. A well-defined parameterization is singularity-free in the neighborhood that is searched during an optimization. There are different possibilities for a parameterization of T.

A translation describes the position component of the pose and is defined by a 3-component displacement vector $\mathbf{t} = (t_x, t_y, t_z)$. There are various ways to parameterize rotations in 3D space, e.g., via Euler angles, unit quaternions or the axis-angle

representation. In this work, unit quaternions are used for the parameterization. Euler angles are later required to interpret the results of the reconstruction experiments. The uniform scaling, in case it needs to be estimated, is defined by a scalar s.

Euler Angles Given three angles $(\theta_x, \theta_y, \theta_z)$, rotations using Euler angles are described by a consecutive sequence of rotations around the three coordinate axes. The order of the rotation influences the outcome of the rotation. Thus, such a representation of rotations depends on the order in which the rotation over the coordinate axes are combined. There are different conventions depending on which coordinate axes are used in which order (e.g. the z-y-x or the z-x-z convention).

A problem with the use of Euler angles are singularities, so-called gimbal locks, which, for example, occur in case one axis is mapped to another in the course of applying a sequence of rotations. Moreover, a parameterization of rotation with Euler angles suffers from discontinuities. To avoid these problems, there are alternative ways to represent rotations, like the axis-angle representation, which describes rotations by one rotation axis with the rotation angle given by the magnitude of that axis. Another alternative are unit quaternions, which are used in this work and will be briefly introduced.

Quaternions Quaternions are generally defined in the form of

$$q = q_w + iq_x + jq_y + kq_z, \tag{4.1}$$

where q_w is a real scalar, q_x, q_y, q_z are real coefficients and i, j, k are imaginary numbers for which

$$i^2 = j^2 = k^2 = ijk = -1 \tag{4.2}$$

applies. Unit quaternions, which satisfy the condition $|\mathbf{q}| = \sqrt{q_w^2 + q_x^2 + q_y^2 + q_z^2} = 1$, can be used to describe spatial rotations of 3D points in space continuously. In this context quaternions are commonly defined as a 4-component vector consisting of a real part $q_w = s$ and the imaginary part $\mathbf{r} = (q_x, q_y, q_z)$ of a quaternion

$$\mathbf{q} = (s, \mathbf{r}) = (\cos\frac{\theta}{2}, \mathbf{u}\sin\frac{\theta}{2}), \tag{4.3}$$

where θ denotes the rotation angle and $\mathbf{u}$ is an unit vector that represents the axis of the rotation. Then, given a point $\mathbf{p} = (p_x, p_y, p_z)$, $\mathbf{p} \in \mathbb{R}^3$ that is represented by a quaternion $\mathbf{q}_p = (0, \mathbf{p})$, a rotation can be performed by a simple vector multiplication

$$\mathbf{q}'_p = \mathbf{q}\mathbf{q}_p\mathbf{q}^{-1}. \tag{4.4}$$

Then, $\mathbf{q}'_p = (0, \mathbf{p}')$ is the transformed point.

With quaternions, a rotation is represented in 4D instead of 3D space. The two quaternions $\mathbf{q}$ and $-\mathbf{q} = (\mathbf{r}\sin(\theta/2 + \pi), \cos(\theta/2 + \pi))$ represent the same rotation, thus, unit quaternions cover a corresponding 3D rotation twice. This avoids singularities, like gimbal locks, or discontinuities, which are a problem when using Euler angles.

For these reasons, quaternions are used in the scope of this work. Accordingly, the rotation component of T is denoted as $\mathbf{q} = (q_w, q_x, q_y, q_z)$. A disadvantage of quaternions is that they are hard to visualize, which is why rotations are converted to Euler angles $(\theta_x, \theta_y, \theta_z)$ to interpret results of the pose reconstructions in Chapter 6.

4.3 Statistical Shape Models

Statistical shape models (SSMs) were first introduced by Cootes et al. [CTCG95]. The idea behind SSMs is to derive deformable models that exhibit two counteractive properties. SSMs are *specific*, in the way that deformations of the model are characteristic of the specific class of shapes the model represents. At the same time, they should be *general* enough to model considerable shape variations of, for instance, the differences of an anatomical structure between different individuals.

An SSM is a linear model that captures the typical shape of a class of shapes along with its variability. Such a model is generated or 'learned' from a statistical analysis of a set of shape examples (*training shapes*) that represent the same class of shapes. SSMs can be used to create new and plausible instances of shapes, similar to those of the training shapes, since only deformations according to the variability within the set of training shapes are permitted.

4.3.1 Statistical Shape Modeling

Before an SSM can be derived, the training shapes need to be converted into a comparable form, which allows for a statistical analysis.

Representing Training Shapes Shapes of the training set are represented by sets of annotated points that sample the boundary of the respective shape. Each point $\mathbf{x}$ possesses one corresponding point $\mathbf{x}' \leftrightarrow \mathbf{x}$ on each of the training shapes. Point correspondences need to be consistent throughout all the shapes in the training set. The point annotations, however, can differ in their nature. They may describe landmarks of distinct biological or anatomical relevancy, mark points with characteristic features (e.g. specific curvature), or could simply be placed to ensure a dense and regular sampling of the shapes. SSMs were also introduced under the name *point distribution models* (PDMs), since the spatial distribution of the annotated points is analyzed in order to generate such a model.

Let n be the number of training shapes and m the number of corresponding points, then the i-th training shape is a vector

$$\mathbf{v}_i = (x_{i1}, y_{i1}, z_{i1}, ..., x_{im}, y_{im}, z_{im})^T, \quad i = 1, ..., n \tag{4.5}$$

of points $\mathbf{x}_{ij} = (x_{ij}, y_{ij}, z_{ij})^T$, $j = 1, ..., m$, where $\mathbf{x}_{ij} \in \mathbb{R}^3$ and $\mathbf{v}_i \in \mathbb{R}^{3m}$. Now, each training shape $\mathbf{v}_i$ can be seen as a single point in $3m$-dimensional space.

Correspondence Problem To establish correspondences between two shapes S_i and S_l, a bijective function $c : S_i \leftrightarrow S_l$ needs to be determined, that defines a set of corresponding points $\mathbf{x}_{ij} \leftrightarrow \mathbf{x}_{lj}$, such that each point $\mathbf{x}_{ij}$ on S_i is mapped to

one point $\mathbf{x}_{lj} = c(\mathbf{x}_{ij})$. Both c and its inverse c^{-1} satisfy the property of being continuously differentiable (i.e., S_i and S_l are diffeomorphic).

It is possible to solve the correspondence problem manually by annotating the training shapes accordingly. Since with complex shapes this may not be feasible, it is desirable to solve this problem automatically. This, however, is a difficult task, as the mapping c is commonly non-linear. The correspondence problem can be solved via geometric surface matching methods. Among various methods, a surface parameterization approach has been proposed by Lamecker [Lam08] and successfully applied to generate statistical shape models. It is based on a consistent decomposition of surfaces into regions, which are homeomorphic to discs.

Shape Alignment To perform a statistical analysis, with the goal to capture shape variation only, it is necessary to remove variation within the training set that is due to transformations related to pose, i.e., translation, rotation, and uniform scaling. To this end, the training shapes have to be aligned with respect to a common coordinate frame. A common algorithm used for this is the Procrustes analysis [Gow75], which iteratively aligns shapes such that the sum of squared distances between corresponding points is minimized. For each shape $\mathbf{v}_i$ the distance

$$E_i = \min_{T_i} \sum_{j=1}^{m} \|T_i(\mathbf{v}_{ij}) - \mathbf{v}_j\|^2 \tag{4.6}$$

is minimized, where T_i is a linear transformation and $\mathbf{v}_j$ are the points of a reference shape $\mathbf{v}$ to which all $\mathbf{v}_i$ are aligned. Initially, $\mathbf{v}$ is one shape of the training set (e.g. $\mathbf{v}_1$). The alignment is then iteratively improved by fitting all $\mathbf{v}_i$ to the current mean shape $\overline{\mathbf{v}}$ (cf. Eq. 4.7) until convergence.

Modeling Shape Variation via Principle Component Analysis An SSM is generated via principle component analysis (PCA) [Shl05, Jol02] on the set of n training shapes $\mathbf{v}_i (i = 1, ..., n)$. PCA is a well-studied technique for dimension reduction of higher dimensional data, which yields a more compact and comprehensible representation of that data. It is based on the assumption that there is noise and redundancy present within a data set, which can be filtered out.

Samples of the data set (our training shapes) are distributed in $3m$-dimensional space, each sample forming one point. The covariance between these points is considered the relationship of interest to be analyzed. Thus, the goal of PCA is to compute the directions of the largest variance, the *principle components*, of the point distribution. This can be achieved by finding a new orthogonal basis to represent the space in which the data set lies in. The basis is determined by finding the eigenvectors of the covariance matrix of the training shapes.

To perform PCA on the training shapes the mean shape

$$\overline{\mathbf{v}} = \frac{1}{n} \sum_{i=1}^{n} \mathbf{v}_i \tag{4.7}$$

is computed at first. The symmetric covariance matrix $\mathbf{C} \in \mathbb{R}^{3m \times 3m}$ is then given

by

$$\mathbf{C} = \frac{1}{n-1}\sum_{i=1}^{n}(\mathbf{v}_i - \overline{\mathbf{v}})(\mathbf{v}_i - \overline{\mathbf{v}})^T. \tag{4.8}$$

If $v_{ik}(k = 1, ..., 3m)$ and $v_{il}(l = 1, ..., 3m)$ are two elements of $\mathbf{v}_i$ with $k \neq l$, then the *diagonal* entries of $\mathbf{C}$, $C_{kk} = \frac{1}{n-1}\sum_{i=1}^{n}(v_{ik} - \overline{v}_k)(v_{ik} - \overline{v}_k)$, are the variance of v_{ik} in all $\mathbf{v}_i$; and the *off-diagonal* entries, $C_{kl} = \frac{1}{n-1}\sum_{i=1}^{n}(v_{ik} - \overline{v}_k)(v_{il} - \overline{v}_l)$, are the covariance, i.e., the degree of correlation between v_{ik} and v_{il}. The aim is to reduce redundancy (indicated by a high correlation of the data, measured via covariance) and to increase the variance to remove noise (indicated by a small variance). This corresponds to finding a matrix of N orthonormal eigenvectors $\mathbf{p}_k$(k=1,...,N) that diagonalize the symmetric matrix $\mathbf{C}$ such that

$$\mathbf{C}\mathbf{p}_k = \lambda_k \mathbf{p}_k. \tag{4.9}$$

Then, regarding the orthogonal basis, all covariance entries satisfy $C_{kl} = 0$, which means that there is no correlation between the elements of $\mathbf{C}$. Each eigenvector $\mathbf{p}_k$ constitutes a *mode of variation*, where the corresponding eigenvalue λ_k specifies the degree of variance in the direction of $\mathbf{p}_k$. The eigenvalues are sorted according to the size of λ_k with

$$\lambda_k \geq \lambda_{k+1}.$$

Consequently, the $\mathbf{p}_k$ with the largest λ_k corresponds to the direction of the largest variance within the data set. Then, a shape lying in the *model space*, which contains all the training shapes, can be represented by the mean shape $\overline{\mathbf{v}}$ and a weighted sum of the eigenvectors

$$\mathbf{v} = \overline{\mathbf{v}} + \mathbf{P}\mathbf{b}. \tag{4.10}$$

$\mathbf{P} = (\mathbf{p}_1, ..., \mathbf{p}_t)$ is a matrix containing a subset of the t most significant eigenvectors; the vector of weights is denoted by $\mathbf{b} = (b_1, ..., b_t)^T$. It is possible to efficiently compute a set of n eigenvectors in case $n < 3m$ [CTCG95]. As Eq. 4.7 implies a linear dependency

$$0 = \frac{1}{n}\sum_{i=1}^{n}\mathbf{v}_i - \overline{\mathbf{v}}$$

the maximum number of linearly independent eigenvectors is $n - 1$.

The SSM used in this work is derived from Eq. 4.10 as a parametrized model $S(\mathbf{b}, T)$ that captures the average shape of the training set as well as its variability in terms of $n - 1$ modes of shape variation (*shape modes*) and is defined as

$$S(\mathbf{b}, T) = T(\overline{\mathbf{v}} + \sum_{i=1}^{n-1} b_i \mathbf{p}_i). \tag{4.11}$$

The degrees of freedom of the SSM are, besides its shape weights $\mathbf{b}$ that control the shape variation, a linear transformation T describing the model's pose. More precisely, T is composed of translation and rotation parameters as well as an uniform scaling (cf. Sect. 4.2.1).

4.3.2 Quality Requirements for SSMs

According to [CTCG95, Dav02], the quality of an SSM is measured by the following criteria:

- Specificity
- Generalization ability
- Compactness

A high specificity of an SSM ensures that the shape instances created with the model are legal representatives of the distinct class of shapes that the model represents. In other words, the model space is reasonably restricted.

In contrast to this, the generalization ability demands that it is possible to generate shapes different from those in the training set. This property allows for the representation of the considerable variation, that is naturally present in a population of shapes of the same class. How well a model generalizes can be determined by means of cross-validation tests. Popular among these is the *leave-one-out* test, which assesses the ability of the model to describe unseen data by excluding one training shape during the model generation process, and fitting the model to this excluded shape. This is repeated for each training shape.

The compactness of a model is measured by the number of parameters required to define the model space. A compact model possess the minimum number of shape modes needed to describe any shape instance.

4.3.3 Fields of Applications

SSMs are applied in various fields related to medical planning and diagnosis. In form of active shape models, they are widely used for the image reconstruction of tomographic data, e.g., for the segmentation of the pelvis [SKH+08] or the liver [KLL07] from CT-data. SSMs can assist in the detection and classification of pathologies, like malformations [BMDDG05] or fractures [RCPA07].

Comprising shape knowledge of a specific class, SSMs are especially suited to provide missing information in a plausible way. They are applied for such purpose in the 3D reconstruction of pathological or missing structures to perform pre-operative surgical treatment planing [ZLES05, Lam08]. In the context of this work, the application of SSMs to the 3D reconstruction from projective data [FL99, LWH06, Zhe06, BMDDG05, MBF+06] is of particular interest, since this way, indispensable 3D knowledge is introduced into the reconstruction process.

4.4 Projection of SSMs

The following section, deals with the geometry used to create projection images. After a concise review of how to generally describe perspective projections, the projection of an SSM is defined.

Projection Geometry A common mathematical model to represent perspective projections is a finite camera in form of a simple pinhole camera model. A detailed introduction can be found in [HZ04].

Cameras represent central projections that map the 3D object space to a 2D image space. More precisely, a 3D point $\mathbf{X} = (X, Y, Z)^T$, $\mathbf{X} \in \mathbb{R}^3$ in an object (or world) coordinate system $\mathbf{W}$ is projected to a point $\mathbf{x} = (x, y)^T$, $\mathbf{x} \in \mathbb{R}^2$ on a 2D image plane via a linear transformation.

The geometric representation of a camera model encompasses the camera's optical center $\mathbf{O}$, i.e., the center of the projection source, and an image acquisition plane I at a distance f (see Fig. 4.2). f is the focal length between $\mathbf{O}$ and I along the principle axis $\mathbf{a}$, which is perpendicular to I and intersects $\mathbf{O}$ as well as the principle point $\mathbf{p} = (p_x, p_y)^T$ in I. The mapping of a point $\mathbf{X} \in \mathbb{R}^3$ to a point $\mathbf{x} \in \mathbb{R}^2$ is defined by the relationship $f/Z = x/X = y/Y$, such that the coordinates of $\mathbf{x}$ are

$$(x, y)^T = (f\frac{X}{Z} + p_x, f\frac{Y}{Z} + p_y)^T. \tag{4.12}$$

A projection can then be expressed in terms of a linear mapping $\mathbf{x} = P\mathbf{X}$ between the object coordinate $\mathbf{X}$ and the image coordinate $\mathbf{x}$. This can be denoted as a matrix multiplication of homogeneous coordinates

$$P\mathbf{X} = \begin{pmatrix} f & 0 & p_x & 0 \\ 0 & f & p_y & 0 \\ 0 & 0 & 1 & 0 \end{pmatrix} \begin{pmatrix} X \\ Y \\ Z \\ 1 \end{pmatrix} = \begin{pmatrix} w \cdot x \\ w \cdot y \\ w \end{pmatrix}, \tag{4.13}$$

where P denotes the *camera projection matrix*. From this projection matrix P, a matrix

$$K = \begin{pmatrix} f & 0 & p_x \\ 0 & f & p_y \\ 0 & 0 & 1 \end{pmatrix} \tag{4.14}$$

can be extracted, called the *camera calibration matrix*, such that $P = K(I_{3\times3} \;\; \mathbf{0}_{1\times3})$ with $I_{3\times3}$ denoting the unit matrix. K comprises the *intrinsic* parameters of the camera.

In addition, the camera model consists of *extrinsic* parameters (a rigid transfor-

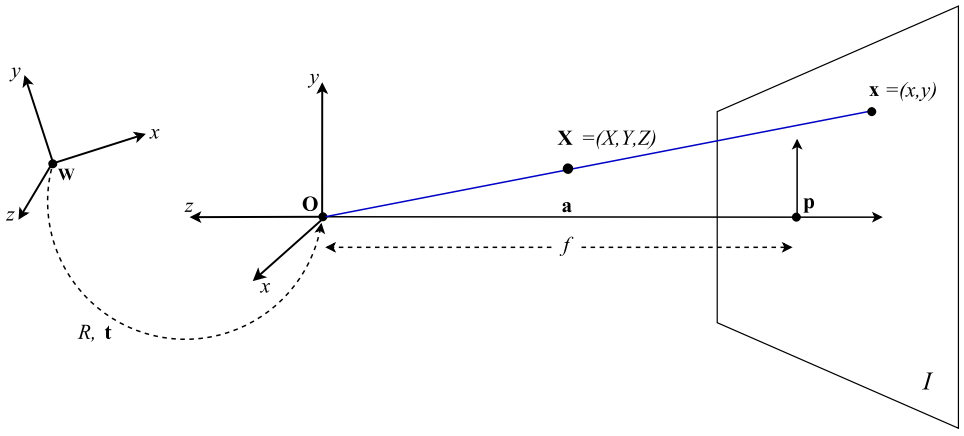

Figure 4.2: Illustration of the camera model to generate perspective projections.

mation T) that relates the camera's coordinate frame to the object coordinate frame $\mathbf{W}$ in which each $\mathbf{X}$ is expressed. A point $\mathbf{X}$ in the object coordinate frame is related to the same point $\mathbf{X}_c$ in the camera coordinate frame by

$$\mathbf{X}_c = R\mathbf{X} + \mathbf{t}, \tag{4.15}$$

where R and $\mathbf{t}$ denote a rotation and a translation, respectively. To represent the alignment of object coordinate system and camera coordinate system, the camera projection matrix is extended to

$$P = K\,(I_{3\times 3} \;\; \mathbf{0}_{1\times 3})\,T = \begin{pmatrix} f & 0 & p_x & 0 \\ 0 & f & p_y & 0 \\ 0 & 0 & 1 & 0 \end{pmatrix} \begin{pmatrix} R_{3\times 3} & \mathbf{t}_{1\times 3} \\ 0_{3\times 1} & 1 \end{pmatrix}. \tag{4.16}$$

Binary Projection Images of the SSM The reconstruction of a 3D shape from 2D projection images is based on the comparison of the projection of an SSM to the given reference images. For this purpose, instances $S(\mathbf{b}, T)$ of the SSM with varying shape parameters $\mathbf{b}$ and transformation T are projected.

In this work, the projection image $I_m : \mathbb{R}^2 \to \mathbb{R}$ of the model $S(\mathbf{b}, T)$ is generated by means of rays that are emitted by a point source and propagated onto an image acquisition plane. The calibration K of the projection source with respect to the image plane is known and is consistent with the camera calibration that was used for the acquisition of the reference image $I_r : \mathbb{R}^2 \to \mathbb{R}$. If the path of a ray to the image plane intersects a simplex V, E or F of the triangulated surface, which represents the SSM, then $I_m(\mathbf{x}) = 1$, where $\mathbf{x} \in \mathbb{R}^2$ is the projected intersection. Otherwise, $I_m(\mathbf{x})$ is set to zero. The projected SSM is then defined as

$$P = \{\mathbf{x} \in \mathbb{R}^2 : I_m(\mathbf{x}) > 0\}. \tag{4.17}$$

The mean shape $\overline{\mathbf{v}}$ of an SSM and its projection images are shown in Fig. 4.3.

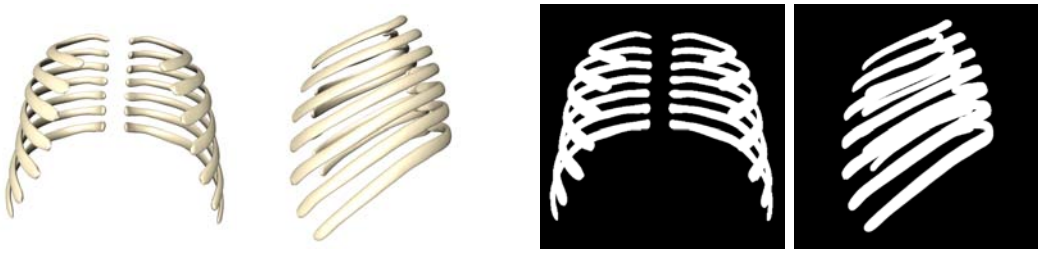

(a) (b)

Figure 4.3: Projection of an SSM: (a) shows the average shape $\overline{\mathbf{v}}$ of an SSM and in (b) binary projection images of $\overline{\mathbf{v}}$ are depicted.

4.5 Optimization

The reconstruction process is defined in terms of an optimization problem. The goal is to determine values for both the shape weights $\mathbf{b}$ and transformation parameters

T of the SSM such that the projection image I_m of the 3D model $S(\mathbf{b}, T)$ is an optimal approximation to the reference image I_r. The model $S(\mathbf{b}, T)$ then serves as an estimate for the 3D shape and 3D pose of the individual rib cage's anatomy at the time of the image acquisition. The quality of the approximation is measured via an objective function $D : \mathbb{R}^d \to \mathbb{R}^+$, where $d = d_T + d_b$ with d_T the number of transformation parameters T and $d_b = n - 1$ the number of shape weights $\mathbf{b}$. Hence, the goal is to compute

$$\mathbf{v}^* = (\mathbf{b}^*, T^*) = \arg\min_{\mathbf{b},T} D(\mathbf{b}, T), \quad \mathbf{v} \in \mathbb{R}^d. \tag{4.18}$$

By minimizing D, the similarity between the reference images and the projections of $S(\mathbf{b}, T)$ is maximized.

To provide a solid basis for the optimization, the parameterization of the search space needs to be well defined, i.e., is singularity-free in the neighborhood that is searched during the iterative optimization and ideally minimal in the sense that as few as possible parameters are used. The shape of the 3D model is parameterized in a well-founded manner by the shape weights $\mathbf{b}$ of the SSM, whose compactness complies with the demand of a minimal parameterization. There parameterization T was defined in Sect. 4.2.1.

4.5.1 Gradient Descent

The objective function D depends on the specific data and thus may exhibit a highly complicated behavior with many local minima. There is no general rule how to treat such non-convex problems. Applying local minimization schemes requires additional suitable heuristics to guide the minimization into the right direction.

For the minimization of D, a gradient-based optimization procedure was adapted [Roh00]. Starting initially at $\mathbf{v}_0 = (\mathbf{b}_0, T_0)$, during step i of an iterative process, the gradient ∇D is approximated at the current solution $\mathbf{v}_i$. Performing a line search along the direction of ∇D, an improved solution $\mathbf{v}_{i+1}$ is computed. This is repeated until a termination criterion is reached: if $\|\nabla D\|$ falls below a certain threshold at a step n, the iteration is stopped, and $\mathbf{v}^* = \mathbf{v}_n$ is the final solution.

The line search is performed as follows: An initial large length parameter δ_0 and a minimal, final parameter δ_f are defined by the user. ∇D is scaled to δ_0 with regard to its maximal component,

$$\mathbf{d} := \frac{\delta_0}{\|\nabla D\|_\infty} \nabla D. \tag{4.19}$$

The step size is then defined by $\|\mathbf{d}\|$. As long as the value of D improves, another step is taken in this direction. Hereafter, the line search is refined with step sizes δ_j iteratively reduced by a constant factor, starting from the current solution: In each iteration, one step is taken in the direction of $\pm\nabla D$. This is repeated until step size δ_f is reached.

Large steps in the beginning of the line search contribute to a faster convergence and prevent the optimization of getting stuck in small local minima, introduced by noise in the data. By narrowing the search interval with reduced step sizes, the neighborhood of a minimum is sampled with increasing accuracy. However, even with these heuristics, the optimization is still local in nature and cannot detect a

global optimum. Therefore, a good initialization is of particular importance (cf. Sect. 5.4).

For a comprehensive introduction to the theory and methods of nonlinear and non-constraint optimization problems, the reader is referred to [Alt02]. This work does not focus on the development of optimization procedures. Thus, the existing technique described above was adopted and found suitable for the needs of the reconstruction problem.

4.5.2 Multilevel Approaches

The basic idea behind a multilevel approach is to start with a simplified version of the problem, such that it is more likely to find a good solution. Then, this initial level is gradually refined until the full problem is reached. There are different possibilities to realize multilevel schemes in practice. The iterative adaptation of the step size, as described in the previous section, is one example.

Data Pyramid Another option is to reduce the resolution of the data, in this case the sampling density of the projection images. By using a coarser representation, a reduced number of data points need to be evaluate to compute the objective function D. According to the current data level, projections can be generated with a lower resolution as well. Both factors can speed up the computation time considerably. Moreover, the influence of noise is reduced and the objective function is smoothed. Hence, the likelihood to get stuck in an undesired local solution is smaller.

Parameter Pyramid The variation of shape $\mathbf{b}$ and pose parameters T of the SSM may lead to similar projections, thus leading to counterintuitive results. Therefore, it seems reasonable to first roughly estimate the parameters of the transformation T before an adaptation of the shape parameters is performed. The multilevel strategies represent different sequences in which certain parameters are optimized. Two different strategies are proposed:

1. An optimization is conducted within the parameter subspace of all parameters of T. Then, the parameter space is extended with all shape parameters b synchronously and an optimization is performed on all the SSM's parameters.

2. The parameter space is consecutively enlarged, starting with the three parameters of the translation $\mathbf{t} = (t_x, t_y, t_z)$, followed by the rotation parameters $\mathbf{q} = (q_w, q_x, q_y, q_z)$ and the scaling parameter s. Finally, the shape weights $b_i \in \mathbf{b}$, sorted according to the significance of their associated shape modes p_i, are successively added to the parameter space.

5 Reconstruction of the Human Rib Cage from X-ray Images

This chapter is devoted to methods that are specific to the application of the 3D pose and shape reconstruction of the human rib cage from projection images. The focus lies on the description of different distance measures to be used as objective functions D for the optimization as described in the previous Chapter, Sec. 4.5. The distance measures were derived to suit the particular needs of the demanding geometry of the rib cage. Strategies to find a suitable initialization are described as well.

5.1 Statistical Shape Model of the Rib Cage

Since projection images can only provide limited information about a 3D anatomy, it is beneficial to incorporate a-priori 3D shape knowledge to infer missing information in an anatomically plausible way. Cootes et al. [CTCG95] proposed SSMs that comprise such shape knowledge (see Sect. 4.3). The reconstruction process is based on an SSM of the human ribs (see Fig. 5.1). It was created from 29 triangulated surface models of different rib cages that were automatically segmented from CT-data [KLvB+07]. The SSM captures the average shape of the training set as well as its variability in terms of $n = 28$ shape modes.

As not all ribs are displayed in each of the CT-images due to an incompleteness of the image data, the model used is restricted to the ribs 2 to 8. The anatomical correspondences between the vertices of the individual surfaces are established during segmentation.

5.2 Distance Measures

Distance measures are generally used to assess dissimilarities between objects. In this work, the distance measure D defined in Sect. 4.5 serves as the objective function for the optimization of the SSM's parameters $\mathbf{b}$ and T (cf. Eq. 4.18). The computation of D is based on the comparison between two images, the reference image I_r and a projection image I_m of an instance of $S(\mathbf{b}, T)$. This image comparison can be defined by a functional

$$E : Y \times Y \to \mathbb{R}^+, \tag{5.1}$$

that quantifies dissimilarities between two images, where Y denotes a set of images $Y = \{I : \mathbb{R}^2 \to \mathbb{R}\}$.

Since the generation of I_m depends on the shape and pose parameters $\mathbf{b}$ and T of the SSM, there is a set of possible images I_m. Consequently, I_m is parameterized by $(\mathbf{b}, T)$ such that $I_m(\mathbf{b}, T) : \mathbb{R}^2 \to \mathbb{R}$.

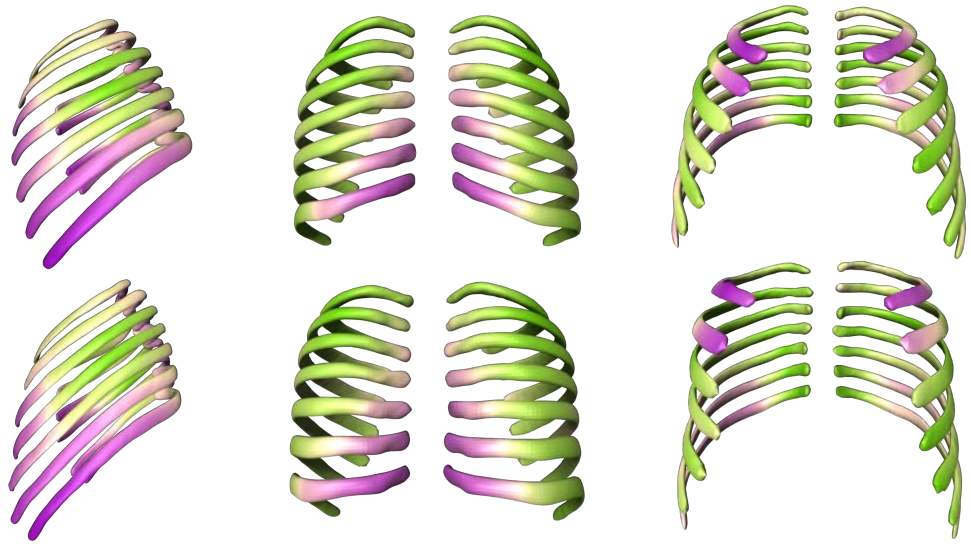

(a) (b) (c)

Figure 5.1: SSM of the ribs: Panels (a), (b), and (c) show the three most significant shape modes with minimal (top) and maximal values (bottom) of the shape weights b_1, b_2, and b_3, respectively. The degree of deformation of different regions are color-coded at the surface, where violet indicates a higher and green a lower deformation. This way, it is intuitive to see which anatomical differences between human rib cages a mode represents, e.g., the inter-patient deviation of the circumference of the upper ribs in the third mode (c).

Then, the objective function is related to the image comparison and specified by

$$D(\mathbf{b}, T) = E(I_m(\mathbf{b}, T), I_r). \tag{5.2}$$

In the following sections, different distance measures are defined, which are to be tested for their suitability for the 3D reconstruction of the rib cage. Different degrees of prior knowledge that could be extracted from X-ray images are considered. Reasons as to when to choose which specific distance measure are motivated and supported by qualitative results in Sect. 6.1.2.

5.2.1 Silhouettes

A silhouette S is a set of contours. The silhouette S_m of the projected SSM P_m in Eq. (4.17) is defined by the boundary ∂P_m and is referred to as the *model silhouette*. The *reference silhouette* S_r in a reference image is assumed to be known.

The distance d_e between silhouettes is defined following the approach of an silhouette-based distance measure as proposed by Lamecker et al. [LWH06]. Given a reference and a model silhouette, the silhouette distance between a contour point $\mathbf{x}_m \in S_m$ to S_r is given as

$$d_e(\mathbf{x}_m, S_r) = \min_{\mathbf{x}_r \in S_r} (\|\mathbf{x}_m - \mathbf{x}_r\|), \tag{5.3}$$

where $\|\mathbf{x}_m - \mathbf{x}_r\|$ is the Euclidean distance between $\mathbf{x}_m$ and $\mathbf{x}_r$,

$$\|\mathbf{x}_m - \mathbf{x}_r\| = \sqrt{(x_{m_1} - x_{r_1})^2 + (x_{m_2} - x_{r_2})^2 + (x_{m_3} - x_{r_3})^2}. \tag{5.4}$$

The distance $d_e(\mathbf{x}_r, S_m)$ from $\mathbf{x}_r$ to S_m is defined analogously.

In case the correspondences between individual rib silhouettes are given, i.e., the ribs are labeled within the images, the distance is defined between contours of these corresponding ribs only. Then, $d_e(\mathbf{x}_m, S_r)$ is defined for a point $\mathbf{x}_m$ in a contour $s_i \in S_m$ to another contour $s_j \in S_r$ with the constraint that $i = j \in \{1, ..., l\}$ applies, where l is the number of labeled ribs.

5.2.2 Symmetric and Asymmetric Distance Measures

The objective function to be minimized can be defined symmetrically or asymmetrically. The symmetric distance measure is given by the integrated symmetric squared distance between two silhouettes S_m and S_r,

$$D_S = \int_{\mathbf{x}_m \in S_m} d_e(\mathbf{x}_m, S_r)^2 d\mathbf{x}_m + \int_{\mathbf{x}_r \in S_r} d_e(\mathbf{x}_r, S_m)^2 d\mathbf{x}_r, \tag{5.5}$$

while the asymmetric distance measure is defined as the integrated squared distance from silhouette S_m to S_r,

$$D_A = \int_{\mathbf{x}_m \in S_m} d_e(\mathbf{x}_m, S_r)^2 d\mathbf{x}_m. \tag{5.6}$$

While the distance D_S is referred to as 'symmetric' the resulting point correspondences that are established between the silhouettes are not symmetric in a mathematical sense (as in bijective), but may be asymmetric (see Fig. 5.2).

5.2.3 Contour Normals

A feature that can assist in finding reasonable point correspondences between silhouette points are the contour normals of silhouettes. As illustrated in Fig. 5.3, orientation differences of the normals at two contour points indicate a mismatch. To avoid contour mismatches, the distance measure is extended to take into account the orientation of the silhouette's normals. The modified distance is then defined as

$$d_n(\mathbf{x}_m, S_r) = \min_{\mathbf{x}_r \in S_r} ((1 + w_e \cdot e)(2 - n)), \tag{5.7}$$

where $n = \mathbf{n}_r \cdot \mathbf{n}_m$ denotes the inner product of two contour normals at points $\mathbf{x}_r$ and $\mathbf{x}_m$, and $e = \|\mathbf{x}_m - \mathbf{x}_r\|$. n serves as a measure of the orientation difference of both normals. Note that $\mathbf{n}_r$ and $\mathbf{n}_m$ are normalized. The purpose of the predefined weighting factor w_e is to balance the impact of the Euclidean distance and orientation difference.

5.2.4 Difference in Area

Another measure, which is proposed to be incorporated into the objective function, is the relative difference of areas of silhouettes. The distance measure is extended

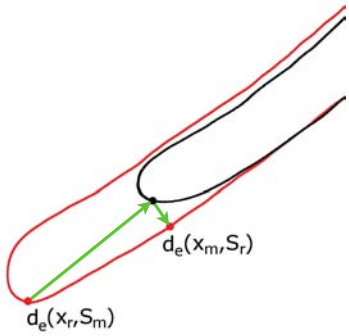

Figure 5.2: Asymmetric point correspondences established using the 'symmetric' (two-sided) distance measure.

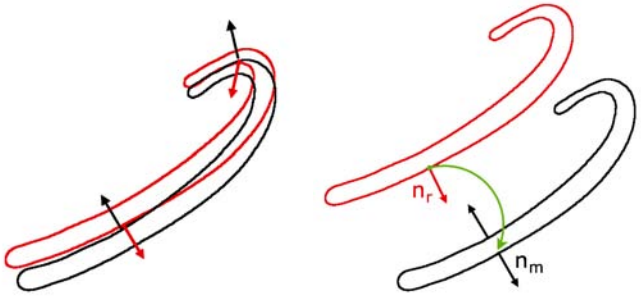

(a) (b)

Figure 5.3: Avoiding contour mismatches: (a) Mismatches can be identified via different orientations of the silhouette normals, (b) whereas the orientation at corresponding contour points is similar.

by a quotient a of the areas A_r and A_m enclosed by the silhouettes S_r and S_m,

$$d_a(\mathbf{x}_m, S_r) = \min_{\mathbf{x}_r \in S_r} ((1 + w_e \cdot e)(2 - n)(1 + w_a \cdot (1 - a))^2), \tag{5.8}$$

where a is given by A_m/A_r if $A_m < A_r$ and A_r/A_m otherwise. The impact of the area difference is controlled by the constant weighting factor w_a and the area of the model projection P_m is defined by

$$A_m = \int_{\mathbf{x} \in \mathbf{P_m}} 1 d\mathbf{x}. \tag{5.9}$$

Given a binary image $L_r : \mathbb{R}^2 \rightarrow \{0, 1\}$ resulting from an segmentation of a reference projection image I_r, where regions of the ribs are labeled with $L_r(\mathbf{x}) = 1$, $\mathbf{x} \in \mathbb{R}^2$, then the area A_r is defined analogously to Eq. 5.9 with $A_r = \int_{\mathbf{x} \in \mathbf{L_r}} 1 d\mathbf{x}$.

5.3 Distance Computation

This section describes implementation details of the computation of the distances d_e and d_n defined in Sect. 5.2.

Silhouette-based Euclidean Distance

Model silhouettes can be obtained automatically from I_m. They are represented as sets of pixels, which define the outer rib boundaries in the rasterized projection image. The outer rib boundaries in the reference images are represented in the same manner. Consequently, the distance measures presented in Eq. (5.5) and Eq. (5.6) are implemented as sums over centers of silhouette pixels. The distance d_e between two silhouettes in Eq. (5.3) is computed by means of 2D distance maps, which encode the Euclidean distance for an arbitrary image pixel to the closest point on a given silhouette. Therefore, for each point $\mathbf{x}_m$ the distance can be retrieved from the distance map of S_r at $\mathbf{x}_m$.

Extended Distances

The normal-extended distance d_n is computed as follows: For a point $\mathbf{x}_m$ with a certain normal orientation $\mathbf{n}_m$, the point $\mathbf{x}_r$ with normal $\mathbf{n}_r$ must be determined that minimizes the combined distance in Eq. (5.7). This $\mathbf{x}_r$ is not necessarily the point in S_r with the smallest Euclidean distance to $\mathbf{x}_m$. For this reason, the distance evaluation cannot be performed by calculating one distance map of S_r as previously described. Instead, a set of Euclidean distance maps $M_i (i = 1, ..., k)$ is computed as follows:

1. For all points in a reference silhouette and a model silhouette the normals are computed. A normal $\mathbf{n}_m$ of a point $\mathbf{x}_m \in S_m$ is given by the normalized image gradient of I_m.

2. All silhouette points are sorted into point sets p_i according to their normal orientation. Therefore, a set of k normalized vectors

$$\mathbf{n}_i = (cos(\varphi_i), sin(\varphi_i))^T \tag{5.10}$$

   is built where $\varphi_i = i \cdot 2\pi/k$ is the orientation angle. A point with a normal $\mathbf{n}_r$ is assigned to the set p_i if $arccos(\mathbf{n}_i \cdot \mathbf{n}_r) \leq \pi/k$ holds true.

3. For each p_i a Euclidean distance map M_i is calculated.

The distance $d_n(\mathbf{x}_m, S_r)$ for a point $\mathbf{x}_m$ is then computed as follows: For each p_i the minimum Euclidean distance e_i of $\mathbf{x}_m$ to p_i is retrieved from the distance map M_i. Then,

$$d_n(\mathbf{x}_m, S_r) = \min_i((1 + w_e \cdot e_i)(2 - \mathbf{n}_m \cdot \mathbf{n}_i)). \tag{5.11}$$

For the area-extended distance d_a the area of a silhouette is given by the number of pixels enclosed by the silhouette contour.

5.4 Initialization

Applying a local optimization scheme as described in Sect. 4.5.1, introduces certain problems in determining a desired reconstruction. Since the objective function D exhibits local minima, it is likely to find local optimal solutions. Two strategies can help to alleviate this problem: One is to strengthen the robustness of the objective function – strategies for this (i.e., to find more meaningful point correspondences between silhouettes) have been proposed in Sect. 5.2. The other one is to determine an initialization near the desired solution.

There are aspects, like the periodicity of similar structures as the ribs and the symmetry of the rib cage, that contribute to the formation of local minima and, hence, should be avoided during initialization. Two approaches are introduced to establish an initial 3D pose of the 3D model prior to the reconstruction process.

Lung Fields

The first approach is based on detecting the pose of the lung's lobes. An initialization using the lung seems reasonable: It gives a good estimation of the rib cage's location, since both structures are anatomically intertwined. Moreover, the lung fields are apparent structures within the radiographs that can be segmented automatically [BvB09].

The initialization consists of fitting a 3D model of a lung to the segmentation of the lung fields within the 2D projection images (see Fig. 5.4). The fitting is performed using the same procedure as proposed for the pose reconstruction of a rib cage (cf. Sect 4.1).

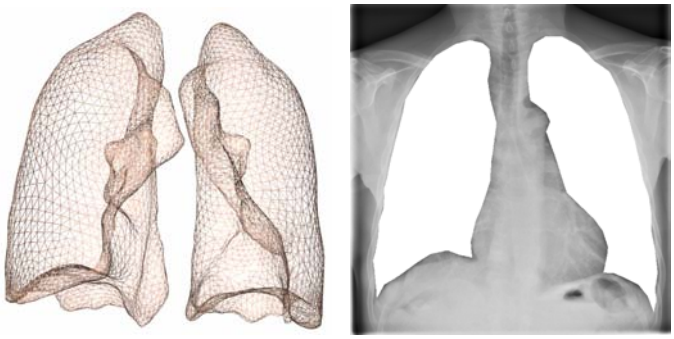

(a) (b)

Figure 5.4: A model of the lung (a) is fitted to the segmentation of the lung fields (b) to roughly estimate the pose of the rib cage.

Subset of Ribs

The idea of the second initialization strategy is to fit a simplified model of the rib cage, consisting only of a subset of ribs, to the image data to initialize the pose. The aim is to overcome the problem of the periodicity of similar substructures within the rib cage model, which may lead to a matching of ribs that do not correspond to each other (e.g. the fourth rib of the model is fitted to the fifth rib in the image data). Moreover, mutual occlusion of the ribs, which could cause a rib on the right to be matched to a rib on the left in lateral projection images, should be prevented.

The ribs corresponding to the subset of the 3D model, that is to be fitted to the image data, need to be segmented in the 2D images. Two different possibilities to choose a suited subset are proposed:

1. Two ribs whose silhouettes are free from occlusion in the lateral image and that are spatially located as far apart from each other as possible in all projection images are used (see Fig. 5.5).

2. A model of two symmetric ribs, sharing the same vertebrae, is adapted to the image data. Both ribs are separately labeled, such that it is possible to distinguish between right and left rib.

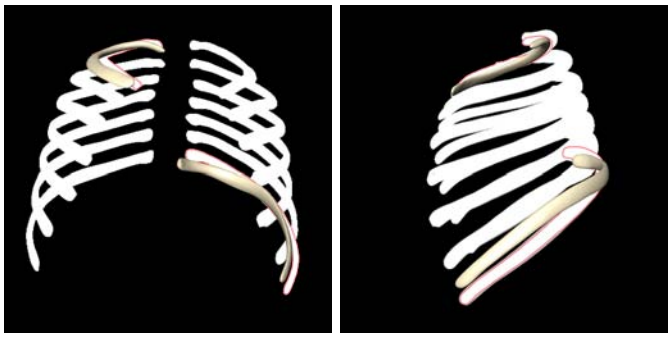

Figure 5.5: A subset of the average SSM is fitted to the segmentation of the corresponding subset in the reference images.

The subset of ribs is extracted from the average shape of the SSM. After the initialization, a subsequent pose and shape reconstruction is performed using the entire set of ribs.

6 Experiments and Results

In the following chapter, a series of experiments is presented alongside with the description of the experimental framework, which was used to test and characterize the performance of the proposed reconstruction approach. After a closer qualitative evaluation of the properties of different distance measures, reconstruction results on artificial projections as well as on X-ray images of a thorax phantom are presented. The reason for using artificial data is that the accuracy of reconstruction results can easily be verified. For *clinical* X-ray images, on the other hand, no ground truth information (like the correct pose and shape of the patient's rib cage) is available. Thus, a verification of the results is very difficult. An option is a visual comparison of the projection images and the 3D model. This, however, is likely to be inconclusive. Another possibility is to compare the outcome of a reconstruction against the results of an alternative method. Unfortunately, the results will be biased due to the error of the method that was used as the basis for comparison. Therefore, a validation is performed with projection images, for which the exact pose and shape parameters to be reconstructed are known (*gold standard*). The validation includes the comparison and evaluation of different distance measure with respect to their applicability to our reconstruction problem.

6.1 Evaluation of Distance Measures

The behavior and robustness of different distance measures was qualitatively investigated to develop predictions about their suitability to be used as objective functions. To this end, an analysis of the parameter space was performed with respect to the free variables of an objective function. The analysis led us to conclusions about the choice of distance measure; it implicated reasonable extensions of the silhouette-based distance measure d_e.

6.1.1 Sampling of the Parameter Space

It is desirable to understand how distinct parameters influence a distance measure and to what extent they contribute to the formation of local minima in the objective function. For this reason, the objective function was sampled in a specified neighborhood along one or more parameters. Given an initial set of parameter values, the parameters in question were iteratively modified (i.e., the values were slightly increased or decreased in a stepwise fashion), whereas the remaining parameters were kept constant. In each step the quality of the current reconstruction was determined by an evaluation of the distance measure.

Various sampling experiments were performed. In most of the experiments, only one parameter was varied and the sampling was performed in the neighborhood of

the desired optimum of the objective function. This enables us to assess the influence of an individual parameter independently from others. Since we are interested in the parameters of the pose in particular, we focus on the analysis of the translation, rotation and scaling parameters. On the following pages, only some selected examples are discussed in this section.

Fig. 6.1 depicts three plots of the respective parameter types for the distance measure D_A, which is solely based on the euclidean distance d_e (Eq. 5.3) between silhouettes. The curves on the left depict the translation along the axes, the curves in the middle correspond to the rotations. For rotations, one of the three components of the quaternion's imaginary part was modified to obtain a rotation around the transversal, sagittal or longitudinal axis. Here, a variation of the quaternion parameters within the interval of $[-0.3, 0.3]$ corresponds to a rotation of up to $\pm 35°$. The scale parameter's curve on the right exhibits a peculiar slight slope for small scale factors, even though all the other parameter are set to the desired optimum. While this effect can be avoided by using a symmetric measure, it can be worthwhile to use an asymmetric measure (cf. Sect. 6.1.2). Consequently, an asymmetric distance measure would have to be modified to better cope with the scaling parameter.

Before this issue is addressed, a distance measure is analyzed, which uses a region-overlap as an alternative to edge-based distances. The measure is defined by the overlap of areas enclosed by the silhouettes of ribs,

$$D_{overlap} = 1 - \frac{A_{intersect}}{(A_r + A_m) - A_{intersect}}, \tag{6.1}$$

where A_m and A_r are the areas of the ribs in model and reference images (as defined in Eq. 5.9) and $A_{intersect} = A - (A - B)$. It can be assumed that the objective function exhibits a more robust behavior regarding the scaling parameter, because a too small scaling results in an reduced area of the model and a poor area overlap, which in turn is penalized by $D_{overlap}$. The curve of the scale factor in Fig. 6.2 indicates that this expectation is met, because the optimum of the scaling possesses a smooth neighborhood and is well pronounced. However, severe problems with the translation and rotation parameters can be observed. Numerous local minima are

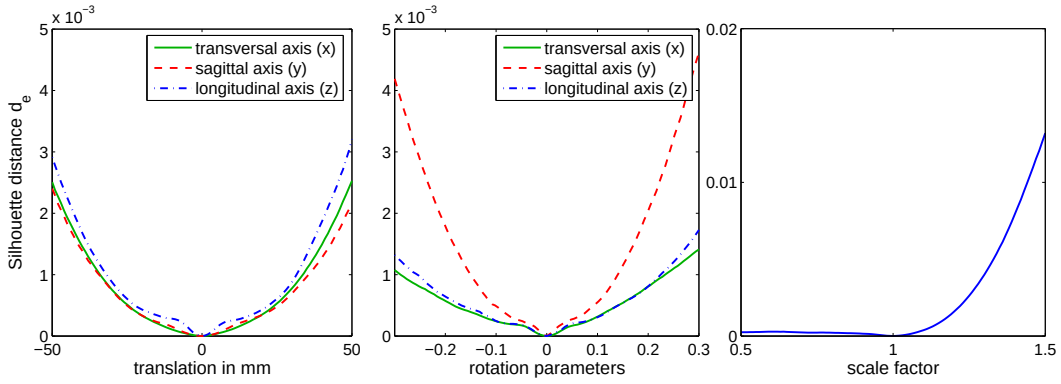

Figure 6.1: Plot of the individual pose parameters in the neighborhood of an optimal reconstruction for distance measure D_A with distance d_e: A scale factor s below the optimal factor has too low an impact on the objective function.

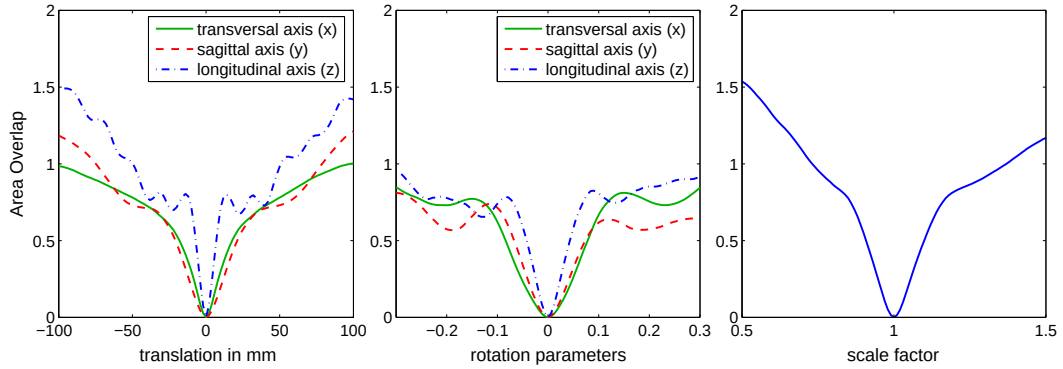

Figure 6.2: The plot of the objective function, that is based on the area overlap $D_{overlap}$, shows a well-defined behavior towards the scaling parameter. However, the objective function exhibits numerous undesired local minima for translation and rotation parameters. Especially the translation along the longitudinal axis is effected.

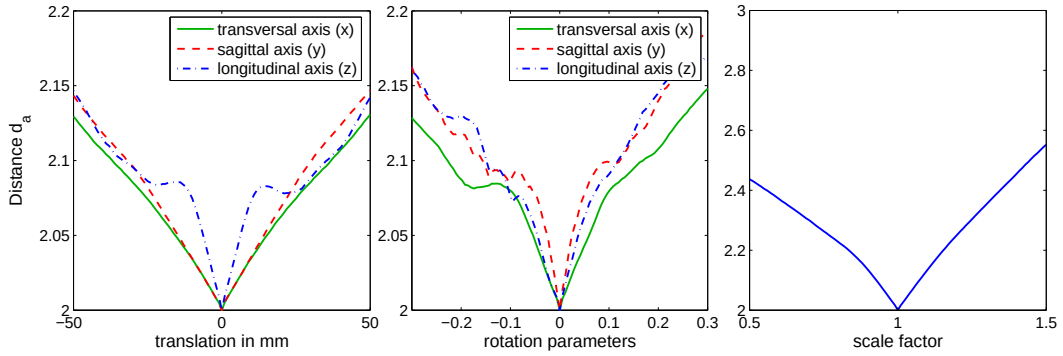

Figure 6.3: Distance d_a exhibits an improved behavior of the scaling in comparison to distance d_e. However, some noise is introduced for the translation and rotation parameter.

present in the vicinity of the desired optimum, in which the optimization can easily get trapped. Especially the curve of the translation along the longitudinal axis is highly jagged. Consequently, considerable differences in the area overlap can emerge, although the translation parameter is only varied slightly. This is the case if the area of ribs in the model images overlap the intercostal spaces between the ribs in the reference images, which is expressed by peaks in the objective function. In addition, the curves of the rotation parameters exhibit undesired local minima, in case the rotation exceeds a deviation from the optimum that is greater than $\pm 15°$. This restricts the range, in which the pose parameters need to be initialized to obtain a successful reconstruction (*capture range*). Therefore, the use of the overlap measure is inadvisable for the reconstruction of the ribs.

With d_a a silhouette-based distance was defined in Eq. 5.8 to better cope with the adaptation of the scaling parameter when using an asymmetric distance measure. The plot of D_A with d_a in Fig. 6.3 shows that the desired optimum of the scaling and its neighborhood are well-defined, which is due to the incorporation of the relative area difference into d_a. Moreover, the plot reveals an improvement in the behavior of the rotation and translation parameters in comparison to $D_{overlap}$. Nevertheless,

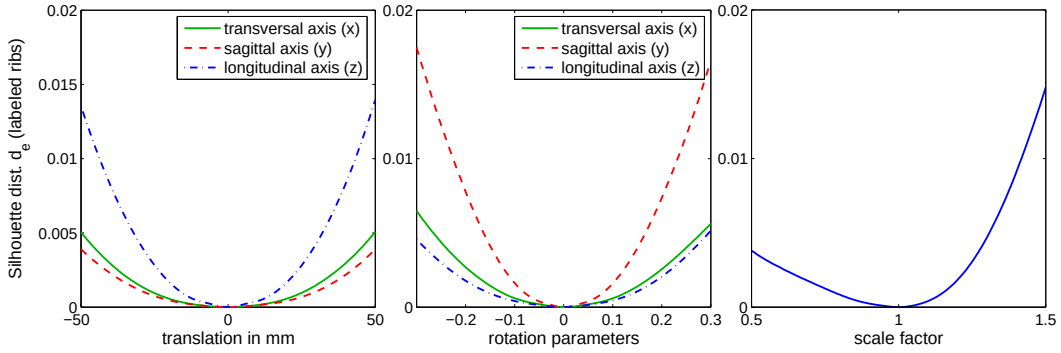

Figure 6.4: Sampling for the distance measure D_A with d_e on ribs that are *labeled* in the reference images: The plots of all pose parameters are characterized by very smooth curves.

local minima are still encountered.

Fig. 6.4 shows the sampling for the distance measure D_A with d_e on ribs that are *labeled* in the reference images. The curves of all parameters, including the scaling, possess a well-defined optimum and are characterized by very smooth curves. This is an indicator that this distance measure is more suited to be used as an objective function.

6.1.2 Choice of Distance Measure

The distance measures defined in Sect. 5.2 are based on silhouettes. For the reconstruction of the rib cage, edge-based features are chosen over region-based features for the following reasons: First, the plots of the objective function based on a region overlap exhibit a difficult behavior as discussed in the previous section. Second, in radiographs the cortical bone layer of the ribs appears reasonably contrasted against the background in regions where the X-rays penetrate the bone surface nearly in a tangential direction. Therefore, the contours of the ribs stand out more clearly and are more easily detectable (cf. Sect. 2.2). Region-based features, on the other hand, are almost non-existent, since the intensity of the inner regions of the ribs hardly differ from the background. Thus, with regard to future clinical applications, edge-based features are used. Motives to choose a particular measure from the different silhouette-based distance measures are given below.

A silhouette-based distance measure (symmetric Eq. (5.5) or asymmetric Eq. (5.6)) is a promising choice for the reconstruction of the pose and the shape of a rib cage, provided that the silhouettes are correctly extracted and the ribs are *labeled* in the reference images. However, tests showed that a silhouette-based distance measure in combination with *unlabeled* rib silhouettes causes erroneous reconstructions. Two problems were identified:

1. *Mismatches of rib contours* can emerge, i.e., ribs are fitted to the contours of two adjacent ribs in the reference images (see Fig. 6.5(a)). This is due to the spatial similarity of the ribs' width and the intercostal space between them.

2. *Mis-assignments of ribs* can occur, caused by the repetition of the ribs in the bone ensemble and the symmetric geometry of the rib cage (see Fig. 6.5(b)).

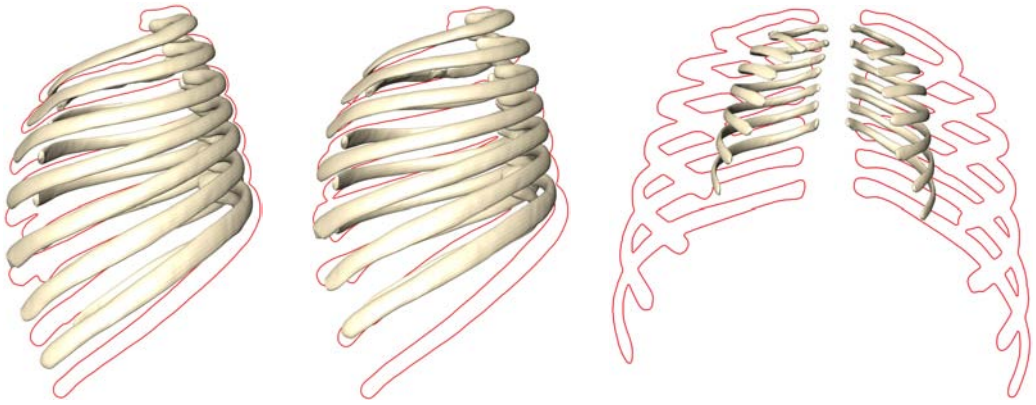

(a) (b) (c)

Figure 6.5: Possible mis-adaptations: (a) With a distance measure D_S and a distance d_e contour mismatches occur, and (b) mis-assignments of ribs appear. (c) In case an asymmetric measure D_A is used, the problem of incorrect scaling is introduced.

Contour mismatches can be avoided by using the normal-extended distance d_n (Eq. (5.7)). Mis-assignments of ribs are more difficult to cope with. Using a symmetric distance measure alleviates, but does not eliminate the effect. This problem was solved by proper automatic initialization that anticipates mis-assignments of the ribs (cf. Sect. 5.4).

The use of *asymmetric* distance measures in combination with unlabeled ribs introduce another problem: the incorrect determination of the scale factor s (cf. Fig. 6.5(c)). The reason for this was illustrated in Fig. 6.1 (right). The plot of the objective function D_A demonstrates that a scale factor below the optimal factor has a very low impact on the objective function, whereas too high factors are accounted for accordingly. Erroneous reconstructions due to too small scale factors are the consequence. Nevertheless, asymmetric distance measures hold the power to better cope with incomplete and erroneous contours within the X-ray images. In case the asymmetric distance measure is applied, the adaptation of the scaling can be controlled by the distance d_a, which incorporates the relative area difference of the silhouettes.

6.2 Reconstruction Accuracy and Robustness

The accuracy of the method was evaluated using the different distance measures described in Sect. 5.2 to assess if the method is applicable to

1. determine *3D pose differences* between images by estimating the 3D pose of a rib cage from projection images, given that the individual 3D rib cage model of the patient is available. Reconstructions of the pose from *two* biplanar, binary projection images (PA and lateral view) as well as from *one* binary PA-projection (see Sect. 6.2.4) were evaluated.

2. perform a *3D shape reconstruction* of an unknown rib cage from *two* biplanar, binary projection images (PA and lateral view), i.e., the simultaneous

reconstruction of the shape and the pose (see Sect. 6.2.5).

6.2.1 Experimental Setup

In order to evaluate the reconstruction quality, 29 surface models of different rib cages (*reference surfaces*) were used, which were extracted from CT-data and previously used for the creation of the SSM.

Reference Images

The reference surfaces were used to generate binary projection images to which the shape model was fitted. All experiments involving shape reconstruction were performed with an SSM, which excludes the shape to be reconstructed from the set of trainings shapes (leave-one-out test, cf. Sect. 4.3.2). The weights $\mathbf{b}$ of all remaining 27 shape modes were optimized. In all experiments involving pose reconstructions, the rib cage models (SSM or non-deformable) were initialized with different, random pose parameters T_0, restricted to the range of ± 30 mm for the translations t_x, t_y, t_z and $\pm 15°$ for the rotation parameters $\theta_x, \theta_y, \theta_z$. The initial scale was restricted to factors between 0.7 to 1.3. The ranges chosen for rotation and scaling follow reasonable pose variations observed during the acquisition of X-ray images in medical practice.

Virtual Image Acquisition

For reconstructions from *two* biplanar images, a PA and a lateral view were used. The camera calibrations for both images were known. The orientation of the lateral projection's source was orthogonal to the PA-view. Its position is given by a 90° rotation of the PA-projection source around the longitudinal axis of the reference surface (see Fig. 6.6). In case a reconstruction was performed from *one* image, only the calibrated PA-view was used. In this virtual setup the distance from the projection sources to the image acquisition plane was $1m$; the angle of the field of view was 22°. In this well-defined setting, the silhouettes of the reference images can be extracted from the binary images as described in Sect. 5.3.

Parameters Setting

The experiments were performed with $k = 16$ distance maps. The weighting factor w_e, ranging from 1 to 65, was found empirically to yield satisfactory results for the different distance measures. The factor for balancing the impact of the relative area difference was set to $w_a = 1$.

6.2.2 Evaluation Measures

The virtual setup described above enables us to verify the accuracy of the reconstruction experiments in 3D because the exact parameters that need to be recovered from the reference images are known. The reference surfaces served as a gold standard for the evaluation of the reconstruction results. The reconstruction quality was measured in 3D via the mean surface distance between the surface of the

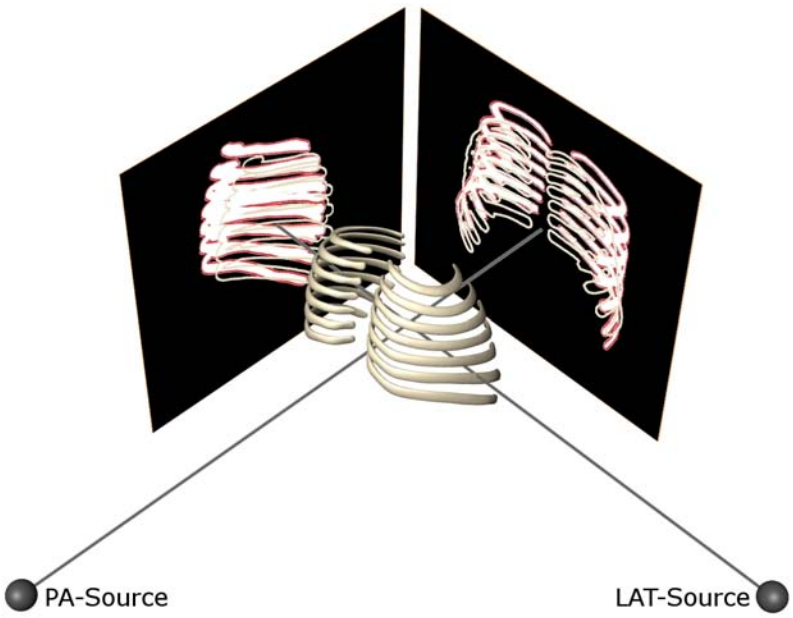

Figure 6.6: Virtual image acquisition setup: the projection sources of the PA-view and the lateral view are calibrated to generate two orthogonal images of the reference surface. A possible initialization of the SSM within this setup is shown: the silhouettes to be matched are those of the projected SSM (beige) and the reference silhouettes (red).

adapted SSM and the reference surface. The surface distance was computed between corresponding vertices of the reference surface and the adapted model. The following reconstruction results are given as average and maximum mean surface distance across the individual reconstructions. The average mean surface distance is computed between each adapted model surface $\mathbf{m}_i \in \mathbb{R}^{3m}$ and a reference surface $\mathbf{r}_i \in \mathbb{R}^{3m}$

$$d_{3D} = \frac{1}{mk} \sum_{i=1}^{k} \sum_{j=1}^{m} \|\mathbf{r}_{ij} - \mathbf{m}_{ij}\|, \tag{6.2}$$

where $\mathbf{m}_{ij} \in \mathbb{R}^3$ and $\mathbf{r}_{ij} \in \mathbb{R}^3$ are the corresponding points. The maximum mean distance represents the worst of the reconstructions (29 for experiments involving shape reconstructions, 20 for pose reconstruction experiments) in terms of its average distance to the reference surface and thereby yields evidence on the robustness of the method. In addition, the error for each transformation parameter was determined to measure the quality of the pose reconstruction. Here, especially the rotational errors are of interest, as the quality of subtraction images is mainly influenced by AP-inclination (θ_x) and rotation around the longitudinal axis (θ_z) [KDM+94]. The transformation error of the reconstructed pose is given by

$$T_{error} = T_{GS} \cdot T_{result}^{-1}, \tag{6.3}$$

where T_{result} denotes the transformation obtained via the reconstruction and T_{GS} is the known pose of the reference surface. The reconstruction results using the respective distances d_e, d_n, and d_a are summarized in Tables 6.2, 6.3, 6.4 and are

discussed in the remainder of this section, after the presentation of experiments to find a suitable initialization.

6.2.3 Initialization

The initialization strategies proposed in Sect. 5.4 were tested using either the 3D model of a lung or a subset of ribs to find an good estimation of the pose prior to the reconstruction process. In each of the following experiments, the 3D model (lung or ribs) was initialized with different, random pose parameters and adapted to a pair of simulated, bi-planar projections in several runs.

Lung Fields Different experiments were performed to test the applicability of an initialization that infers the approximate pose of the rib cage from the adaptation of a lung model to segmentations of lung fields in radiographs, . Two of the experiments, in which the pose initialization was achieved by fitting the given 3D lung to the projections using D_a and the silhouette-based distance d_e, are summarized below:

1. *Ideal conditions*: A patient-specific 3D lung was adapted to the projections of exactly the same lung geometry (i.e., the shape of the lung was known in advance).

2. *Simulation of more realistic conditions*: Regions of the lung that are superimposed by other organs, as heart and midriff, are difficult to detect on radiographs by automatic segmentation methods and vary severely due to respiration and heartbeat. For this reason, a segmentation of the lung from X-ray images exhibits significant differences compared to silhouettes of the model images (see Fig. 6.7 (top)). To simulate the adaption of a lung model to lung segmentations, which differ in the above mentioned manner, reference silhouettes, in which the inner regions of the lung fields were altered to resemble realistic segmentations (see Fig. 6.7 (bottom)), were artificially generated. Only the outer contours (blue contours in Fig. 6.7) of the lung lobes were used for the distance computation.

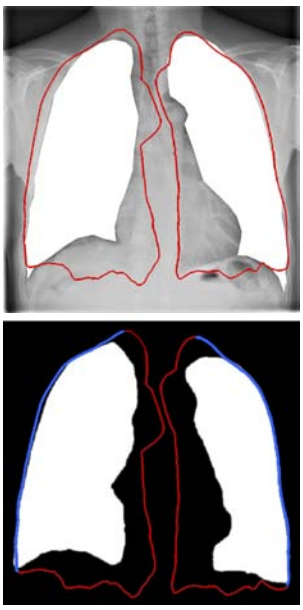

Figure 6.7: Difference between the segmentation of the lung fields (white) and the model silhouette (red): Actual (top) and simulated lung field segmentation (bottom).

The results of both experiments are listed in Tab. 6.1. While the first test yields a precise estimation of the lung's pose, the experiment under more realistic condition leads to an inaccurate pose initialization with translation and rotation errors of up to 11 mm and 13°, respectively.

Subset of Ribs The two initialization strategies proposed in Sect. 5.4, which use a subset of ribs, were tested. The results are summarized in Tab. 6.1. The first

Table 6.1: Results for the initialization experiments: The average reconstruction error is listed for each transformation parameter. Rotation errors are specified by Euler angles in degree, and the averaged mean surface d_{3D} distances with standard deviations (and maximum mean surface distances) are given in millimeter.

Experiment	T_{error}=$(t_x, t_y, t_z, \theta_x, \theta_y, \theta_z, s)$	Surf. dist. in mm
Lung experiment 1, d_e	0.04, 0.05, 0.05, 0.03, 0.02, 0.04, 0.00	0.05 ± 0.01 (0.12)
Lung experiment 2, d_e	2.78, 0.98, 10.7, 11.1, 6.08, 13.1, 0.00	10.6 ± 17.7 (78.4)
2 asymmetric ribs, d_e	2.27, 1.93, 3.68, 2.68, 1.10, 4.47, 0.00	3.05 ± 6.00 (21.2)
2 asymmetric ribs, d_a	0.38, 0.80, 0.24, 0.13, 0.37, 0.86, 0.01	0.56 ± 0.20 (1.15)
Symmetric rib pair, d_a	0.48, 1.15, 0.46, 0.44, 0.66, 0.82, 0.00	0.91 ± 0.24 (1.40)

strategy, involving the adaptation of two asymmetrically arranged ribs to the corresponding segmentations of the two ribs in the reference images, yielded a good pose initialization in case d_a is used (translation errors $\leq$ 0.8 mm and rotation errors $\leq 1°$).

With the second strategy, good initial pose estimations have been obtained as well, in case one of the lower ribs was used (translation errors $\leq$ 0.8 mm and rotation errors $\leq 1.2°$ at the 7th vertebra). An adaptation using a rib pair attached to an upper vertebra led to an inaccurate estimation of the scaling. Lower ribs cover a larger area within the projection images and seem to be better suited for the estimation of the scale factor.

A labeling to distinguish which of the ribs is located on the right or left body side is mandatory using the symmetric rib pair, because in lateral projections, ribs of the same height occlude each other due to the rib cage's symmetry. Therefore, a left rib is easily fitted to the contours of the right rib, and vice versa.

The results indicate that using a subset of ribs leads to better initializations of the pose compared to the strategy based on segmentations of the lung fields. Consequently, subset of ribs are applied, in case a pose initialization is necessary.

6.2.4 3D Pose Reconstruction

Patient-specific rib cage models with different, random pose initializations T_0 were adapted to reference images of the respective rib cage geometry. Only parameters of T are to be determined. Ideally, the surface distance for such pose reconstruction would reduce to zero, since the shape of the rib cage is known. In terms of the reconstruction quality the randomly initialized models deviated on average 21.8 mm (max. 37.4 mm) from the reference surface with the correct pose before the method proposed in this thesis was applied.

In case reconstructions were performed with *two* reference images, the distance d_e in combination with *labeled* ribs led to results with surface distances $\leq$ 0.2 mm and rotation errors $\leq 0.2°$ on average, regardless of whether an asymmetric or a symmetric distance measure was used (see Tab. 6.2). A symmetric measure with distance d_e and *unlabeled* ribs occasionally caused contour mismatches and misassignments of ribs, and it yielded an average reconstruction quality of 2.0 ± 3.0 mm (max. 8.5 mm). With an asymmetric distance d_n applied to the reconstruction of

Table 6.2: Results for the silhouette-based distance d_e. The averaged mean surface distances d_{3D} with standard deviations (and maximum mean surface distances) are given in millimeter. In addition, the average reconstruction error is listed for each transformation parameter. Rotation errors are specified by Euler angles in degree. Experiments using labeled (L) or unlabeled (U) silhouettes of the ribs as well as asymmetric (D_A) or symmetric (D_S) distance measures are listed. For the shape reconstructions leave-one-out tests were performed.

Experiment	Views	Pose		Shape	Pose + Shape	
		Surf. dist.	T_{error}=$(t_x, t_y, t_z, \theta_x, \theta_y, \theta_z, s)$	Surf. dist.	Surf. dist	T_{error}=$(t_x, t_y, t_z, \theta_x, \theta_y, \theta_z, s)$
D_S, L	PA/lateral	0.16 ± 0.06 (0.28)	0.08, 0.18, 0.12, 0.05, 0.14, 0.21, 0.00	2.08 ± 0.96 (4.11)	2.18 ± 0.82 (3.91)	0.40, 0.56, 0.62, 0.61, 0.20, 0.30, 0.00
D_A, L	PA/lateral	0.17 ± 0.07 (0.39)	0.06, 0.21, 0.14, 0.06, 0.13, 0.19, 0.00	2.00 ± 0.87 (4.19)	2.62 ± 1.15 (5.30)	0.60, 0.84, 0.90, 0.80, 0.19, 0.35, 0.00
D_S, U	PA/lateral	1.97 ± 2.98 (8.45)	0.92, 2.31, 2.20, 0.44, 1.26, 1.66, 0.00	2.34 ± 0.98 (4.26)	4.53 ± 2.00 (8.98)	1.27, 3.68, 2.70, 1.85, 1.60, 2.16, 0.00
D_A, U	PA/lateral	19.2 ± 10.9 (38.3)	9.06, 11.5, 35.7, 7.95, 3.64, 4.57, 0.25	2.54 ± 1.36 (7.12)	-	-
D_S, L	PA	0.29 ± 0.21 (0.97)	0.10, 0.57, 0.16, 0.06, 0.09, 0.14, -			
D_S, U, Init.	PA	0.72 ± 0.37 (1.75)	0.25, 1.41, 0.23, 0.13, 0.27, 0.41, -			

Table 6.3: Results for the extended distance d_n.

Experiment	Views	Pose		Shape	Pose + Shape	
		Surf. dist.	T_{error}=$(t_x, t_y, t_z, \theta_x, \theta_y, \theta_z, s)$	Surf. dist.	Surf. dist	T_{error}=$(t_x, t_y, t_z, \theta_x, \theta_y, \theta_z, s)$
D_A, L	PA/lateral	0.37 ± 0.20 (0.81)	0.21, 0.62, 0.37, 0.15, 0.18, 0.26, 0.00	2.00 ± 0.87 (4.34)	2.48 ± 1.04 (5.26)	0.48, 0.99, 0.93, 0.92, 0.30, 0.44, 0.00
D_A, U	PA/lateral	11.1 ± 6.86 (27.4)	4.95, 5.85, 25.8, 7.20, 4.28, 2.58, 0.11	2.53 ± 0.78 (4.26)	-	-

Table 6.4: Results for the extended distance d_a.

Experiment	Views	Pose		Shape	Pose + Shape	
		Surf. dist.	T_{error}=$(t_x, t_y, t_z, \theta_x, \theta_y, \theta_z, s)$	Surf. dist.	Surf. dist	T_{error}=$(t_x, t_y, t_z, \theta_x, \theta_y, \theta_z, s)$
D_A, L	PA/lateral	0.28 ± 0.13 (0.52)	0.11, 0.47, 0.29, 0.10, 0.19, 0.30, 0.00	2.11 ± 0.82 (3.96)	2.85 ± 1.09 (4.99)	1.34, 1.44, 2.03, 1.13, 0.33, 0.52, 0.01
D_A, U	PA/lateral	4.60 ± 3.90 (9.30)	2.03, 5.36, 4.63, 2.33, 2.88, 2.87, 0.00	-	-	-
D_A, U, Init.	PA/lateral	0.55 ± 0.22 (1.15)	0.38, 0.80, 0.24, 0.13, 0.37, 0.86, 0.00	2.53 ± 0.78 (4.26)	4.69 ± 2.35 (12.0)	1.32, 2.85, 2.16, 2.02, 1.02, 2.32, 0.02

unlabeled ribs the additional problem of incorrect scaling occurred (11.0 ± 6.9 mm (max. 27.4 mm)). Here, the scaling s highly deviates with a factor of 0.25 on average from the correct size. The effects of the contour mismatches and incorrect scaling were alleviated (4.6 ± 3.9 mm (max. 9.3 mm)) by using distance d_a. In this case the errors in the parameters T were $\leq 2.9°$ for the rotation and ≤ 5.4 mm for the translation. These errors are due to ribs mis-assignments that occurred in all the experiments with unlabeled ribs. In order to overcome the problem of these mis-assignments, only a subset of ribs is fitted to the image data to initialize the pose. This initialization avoids the periodicity of the ribs and prevents mutual occlusion in the lateral projection image. After such an initialization, a subsequent pose and shape reconstruction was performed using the entire set of ribs. It yielded a surface distance of 0.6 ± 0.2 mm (max. 1.2 mm) and rotation errors below 0.9° for distance measure D_A and distance d_a.

In addition, pose reconstructions from *one* PA-view were carried out. In these experiments, the scale parameter was not optimized, since depth, i.e., translation along the sagittal axis (t_y) and size are redundant. However, this is of little concern for a pose reconstruction, because the size of a rib cage is determined during the prior 3D shape reconstruction. Nevertheless, if two calibrated views are available, adapting the size of a rib cage during a pose reconstruction is possible and has its advantages: A possible scaling error that emerges during 3D shape reconstruction can be compensated for, which may result in an improved reconstruction of the pose.

A drawback of this approach is that calibrated PA and lateral views are needed that represent the same scene. For this reason, it is worthwhile to conduct pose reconstructions from one PA-image. Reconstructions from one PA-view led to an average accuracy of 0.3 ± 0.2 mm (max. 1.0 mm) with labeled ribs and 0.7 ± 0.4 mm (max. 1.8 mm) with unlabeled ribs after a proper initialization using D_S and d_e. The reconstruction qualities of these results are slightly lower in comparison to the respective reconstructions from two views. It is noteworthy that the rotation angles of interest can be recovered with a higher accuracy ($\leq 0.1°$ and $\leq 0.4°$) than from two views. From the translation error along t_y it is obvious that the error is mainly due to a slightly erroneous estimation of the rib cage's projection depth.

6.2.5 3D Shape and Pose Reconstruction

For the evaluation of a simultaneous reconstruction of the shape and the pose it is necessary to know to what extent the SSM can approximate the shape of an unknown rib cage independently from the pose. Hence, the method's ability to assess only the shape of an unknown rib cage with a given correct pose is demonstrated at first. Then, the results of the simultaneous pose and shape reconstruction are presented.

Pose Independent Shape Reconstruction

To assess the optimal value obtainable with the SSM as a reference value, *direct surface optimizations* were performed in 3D by minimizing the distance between the SSM and the reference surfaces. This leave-one-out test resulted in a mean surface distance of 1.6 ± 0.6 mm (max. 2.9 mm).

For the evaluation of the 3D shape reconstruction from 2D image data, the SSM was adapted to 29 pairs of binary reference images with a given, correct pose. All

the shape reconstruction experiments with labeled ribs yielded similar results of approximately 2 mm mean surface distance averaged across the individual 29 reconstructions. Using unlabeled ribs, the reconstruction quality slightly degrades for all distance measures with results ranging from 2.3 to 2.5 mm.

Combined Pose and Shape Reconstruction

For the 3D reconstruction of an a-priori unknown geometry from clinical data. The shape and the pose must be reconstructed simultaneously. To evaluate the method in this context, the SSM was fitted to pairs of reference images of an unknown rib cage using different random pose initializations.

With an average reconstruction quality of 2.2 mm a simultaneous pose and shape reconstruction with labeled ribs using a symmetric measure with distance d_e yielded a result that is comparable to the pose independent shape reconstruction (see Sect. 6.2.5). Reconstruction examples are shown in Fig. 6.9(a) and Fig. 6.9(b). In case only unlabeled rib silhouettes were available the symmetric measure d_e resulted in 4.5 ± 2.0 mm (max. 9.0 mm).

For unlabeled ribs, the distance d_a performed best among the asymmetric measures, since incorrect scaling and contour mismatches were avoided. In this case an initialization of the pose is required. Experiments under these conditions yielded an average reconstruction quality of 4.7 ± 2.4 mm (max. 12.0 mm) (see example reconstructions in Fig. 6.10(a) and Fig. 6.10(b)).

Fig. 6.8 depicts an exemplary result of a simultaneous shape and pose reconstruction from *one* PA-image. While the reconstruction obtains a good match between reference and model silhouette, the lateral 3D view shows that the SSM does neither correctly estimates the shape nor the pose. Consequently, the information of only one projection image is ambiguous and insufficient for the presented method. To rule out such incorrect reconstructions, information from a second image is indispensable.

(a) (b) (c)

Figure 6.8: Shape Reconstruction from one PA-image: Although a good match between reference and model silhouette can be obtained in (a), and the adaptation seems accurate in (b), the 3D view in (c) reveals an incorrect pose and shape reconstruction.

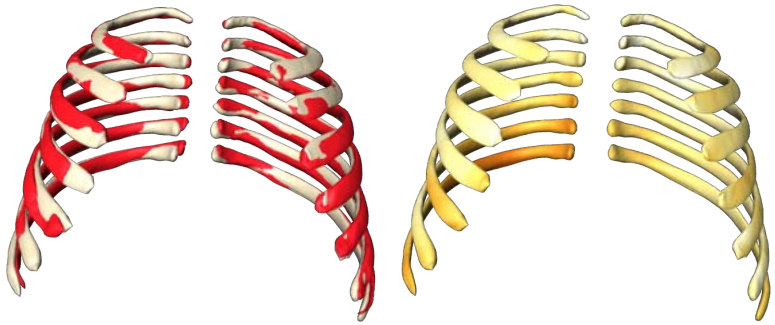

(a) A good result (labeled ribs, D_S, d_e): 2.03 mm

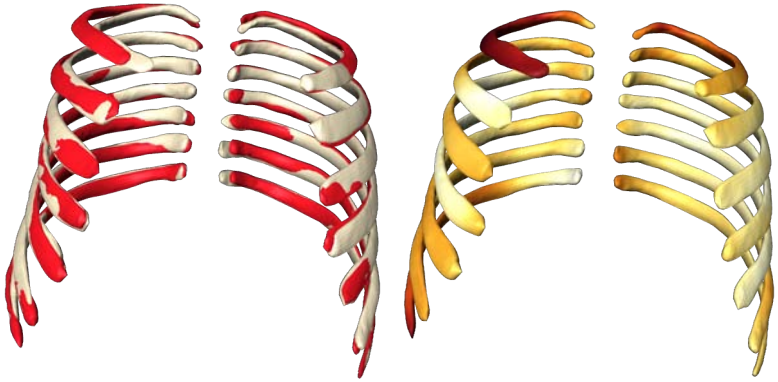

(b) A more difficult case (labeled ribs, D_S, d_e): 2.44 mm

Figure 6.9: Exemplary results of combined pose and shape reconstructions for the most suitable distance measure with *labeled* ribs: For each result both the reference surface (red) and the reconstructed surface (beige) are depicted on the left. The reconstructed surface with its distance to the reference surface is shown on the right. In addition, the average surface distance d_{3D} is given.

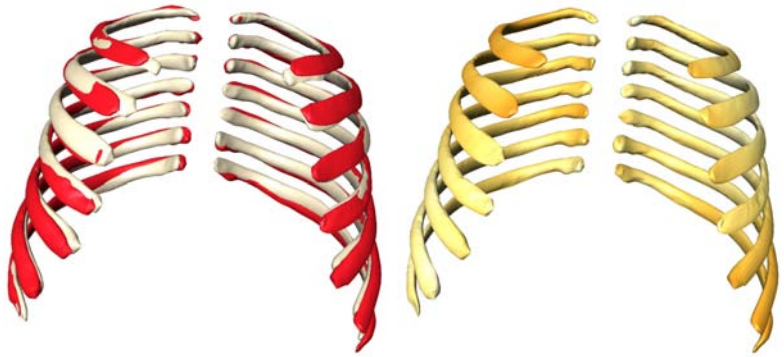

(a) A good result (unlabeled ribs, D_A, d_a, Init.): 1.81 mm

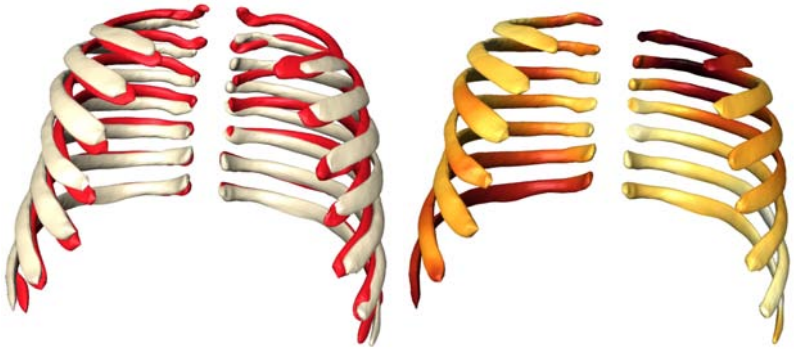

(b) Problematic case (unlabeled ribs, D_A, d_a, Init.): 5.04 mm

(c) Colormap encoding the surface distance.

Figure 6.10: Exemplary results of combined pose and shape reconstructions for the most suitable distance measures with *unlabeled* ribs.

6.3 Reconstruction from Radiographs

The experiments in the previous section were designed to show that reconstructions can be achieved under well-defined conditions. The silhouettes of the reference images are ideal in the sense that they are not affected by errors that are made during the feature extraction. Such errors depend on the image quality and on the chosen algorithm to extract the features, or on the skills and experience of the operator, in case a segmentation is performed manually. To test the reconstruction approach under more realistic conditions, pose reconstructions were obtained from real, manually segmented X-ray images.

6.3.1 X-ray Images of a Thorax Phantom

For evaluating the reconstruction from radiographs, X-ray images of an artificially modeled human thorax (*phantom*) were used. The development of the phantom and the image acquisition was performed by *Philips Research Europe – Medical Imaging Systems* in Hamburg for a study by von Berg et al. [vBMSPN08] to determine the influence of pose differences on temporal subtraction of chest radiographs. The phantom contains real thoracic bones. Muscles, fat and the organs of the thoracic cavity are modeled by plastic. The image acquisition method of the phantom radiographs, which involves the precise positioning of the thorax phantom with a turntable device, allows for the exact modulation and determination of the thorax' pose during image acquisition. In order to verify the reconstruction results from the images, this pose of the thorax was used as gold standard in the following pose reconstruction experiments. Fig. 6.11(a) shows an X-ray image of the phantom.

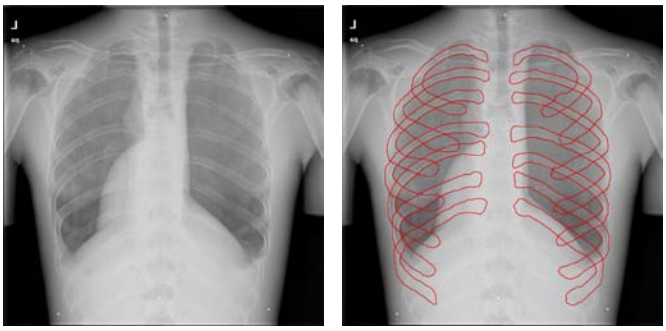

(a) (b)

Figure 6.11: Phantom of a human rib cage: (a) X-ray image of the phantom, and (b) manually produced segmentation of the X-ray image.

6.3.2 3D Pose Reconstruction

Since only PA-images of the phantom were available and the determination of the shape and pose requires two calibrated images (cf. Sect 6.2.5), only the pose of the phantom was reconstructed. A 3D model of the phantom's rib cage was available from a reconstruction of the phantom's CT-data (see Fig. 6.12). The four different X-ray images have been manually segmented (see Fig. 6.11(b)) to obtain reference silhouettes. One of the images is a baseline image, for which the phantom was positioned to obtain a standard PA-view. Images 2 and 3 were acquired with a rotational

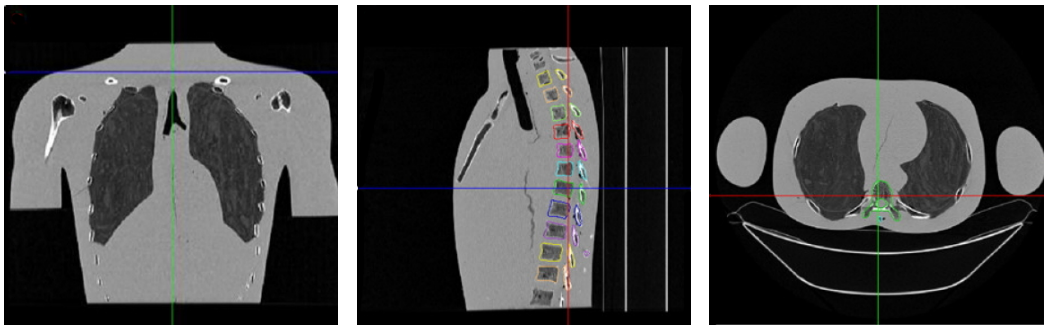

(c) (d) (e)

Figure 6.12: CT-data of the thorax phantom: (a) coronal, (b) sagittal, and (c) axial view (image courtesy of Dr. Jens von Berg).

difference of $\pm 5°$ around the longitudinal axis (θ_z) compared to the baseline image. In image 4 the phantom was positioned to exhibit an AP-inclination of 3°.

For each of the four images, 20 different reconstructions were performed with randomly initialized poses of the phantom's 3D model. Thus the experiments conditions are similar to the pose reconstructions in Sect. 6.2.4, except that the reference silhouettes are error-prone up to a certain degree, due to the manual segmentation of the ribs.

The reconstructions were performed using the distance measure D_S and distance d_e with labeled ribs. A problem that was encountered during a first series of experiments was a mis-adaptation due to a strong PA-inclination of the adapted model. The ribs of the model tend to adapt only to the anterior part of the ribs in reference silhouettes. Four out of 20 reconstructions showed this type of behavior. The erroneous reconstructions were anticipated by weighting the silhouette distances $d_e(x_r, S_m)$ of the posterior parts of the ribs higher then the anterior parts. The average results using the weighting are summarized in Tab. 6.5. Illustrations of two reconstructions are shown in Fig. 6.13. The results indicate that the rotation, in form of the angles $(\theta_x, \theta_y, \theta_z)$, can be estimated with a high accuracy ($\leq 0.3°$).

However, there is some inaccuracy (up to 13.7 mm) with the reconstruction of the translation along the sagittal axis. It is difficult to estimate this parameter, because in contrast to the other translation parameters, a translation along the projection direction (sagittal axis) leads only to a small change in the silhouette. Consequently,

Table 6.5: Results for the pose reconstruction of the phantom geometry from manually segmented PA X-ray images. Distance measure D_S and distance d_e were used. The ribs have been labeled.

Phantom X-ray	Id.	$T_{error}=(t_x, t_y, t_z, \theta_x, \theta_y, \theta_z)$	Surf. dist. in mm
Baseline Image	7	0.22, 6.41, 0.34, 0.17, 0.10, 0.13	2.94 ± 0.74 (3.97)
Image 2, θ_z=+5	12	0.09, 13.65, 0.20, 0.21, 0.10, 0.22	6.40 ± 1.39 (10.80)
Image 3, θ_z=−5	34	0.19, 2.45, 1.04, 0.11, 0.23, 0.10	1.35 ± 0.80 (3.06)
Image 4, θ_x=+3	58	0.07, 11.03, 0.58, 0.22, 0.03, 0.33	5.28 ± 1.69 (10.99)

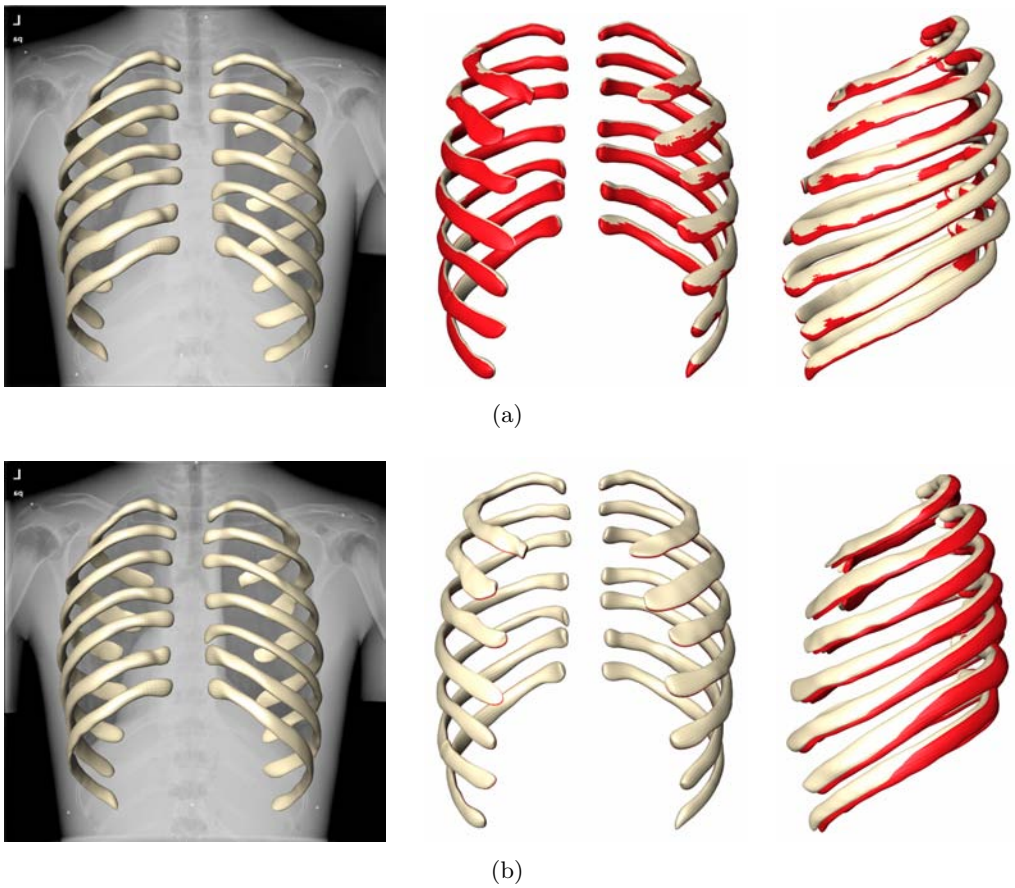

Figure 6.13: Exemplary pose reconstruction results of two phantom images: The reference surface in red illustrates the pose of the phantom during image acquisition; the beige surface shows the reconstruction result. (a) depicts one result of average quality of Image 3 and (b) one result of Image 4, where a slight error in translation along the sagittal axis (-6 mm) can be observed in the lateral 3D view (right).

the impact of the translation is too low on the objective function.

Fig. 6.14 shows the plot of the three translation parameters. In comparison to the other two parameters, the curve of the translation along sagittal axis is less pointy and, thus, the optimum is less pronounced and difficult to determine. The translations along longitudinal and transversal axes, on the other hand, exhibit a good accuracy ($\leq$1.1 mm).

6.3.3 Exemplary Pose Reconstruction from Clinical X-ray Images

To show the potential of the proposed method to be used with clinical X-ray images, pose reconstructions from three different images of a patient were performed. Since no ground truth information was obtained with these images, it is not possible to assess the outcome of the reconstruction results quantitatively. Nevertheless, the visual evaluation of the result can serve as indicator for the reconstruction quality. This, however, is no reliable evidence that a reconstruction was actually successful.

The pose reconstruction of one of the three patient's clinical radiographs is shown

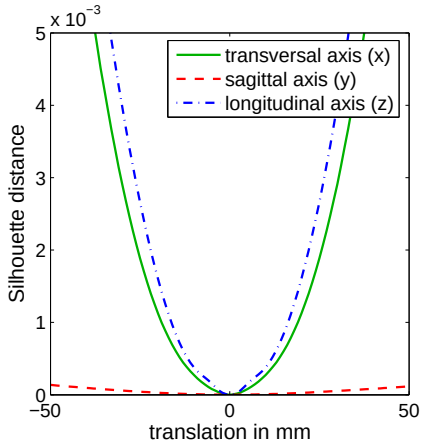

Figure 6.14: Plot of the three translation parameters using a single PA-image: In contrast to transversal and longitudinal axes, the translation along sagittal axis reveals a low impact on the objective function.

in Fig. 6.15. The segmentation of the visible parts of the ribs was obtained manually (see. Fig. 6.15(b)). The 3D shape was available from a reconstruction of the patient's CT-data, since no calibrated, biplanar images were available as a basis for a shape reconstruction. The exemplary reconstructions were performed using distance measure D_S with d_e and labeled ribs.

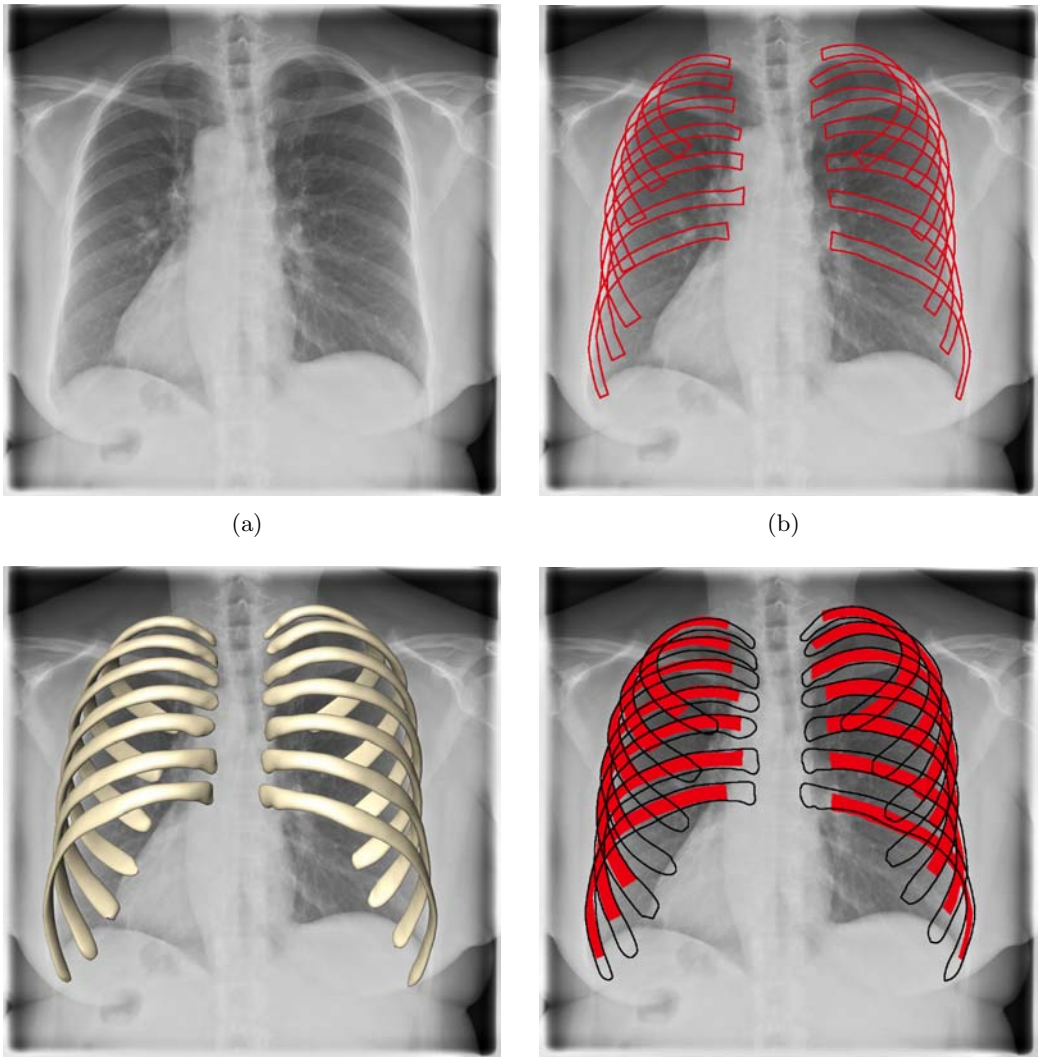

(a) (b)

(c) (d)

Figure 6.15: Pose reconstruction from a clinical X-ray image: (a) and (b) show the X-ray image of a human thorax and a manual segmentation of the visible parts of the ribs. (c) depicts the patient's 3D model (extracted from CT data) with the estimated 3D pose. The segmentation and silhouette of the projected 3D model in (d) exhibit a good match, considering that the endings of the rib could not be segmented properly from the X-ray image.

7 Discussion and Future Work

In this chapter, the results and implications for the applicability of the rib cage reconstruction method to assess pose differences between temporal sequential radiographs are discussed. First, the results achieved with the proposed method are analyzed. Then, the relevance for a clinical application is discussed and an outlook to what should be addressed in future work to meet clinical requirements is provided.

7.1 Methodological Findings

In the following section, the method's performance is analyzed regarding the obtainable reconstruction quality. A high-level overview is given below in Tab. 7.1. Afterwards, the results are compared to other related methods.

7.1.1 Accuracy of Pose Reconstruction

With the proposed method applied to reconstruct the pose from artificial binary projections, rotation errors are below 0.3° on average for all distance measures on *labeled* ribs. On *unlabeled* ribs the pose reconstructions with distance measure D_A with d_a from two views as well as the distance measure D_S with d_e from a single PA-view – both using prior initialization – yield an average accuracy of 0.4°. Hence, for these distance measures the accuracy is sufficient to detect undesirable pose deviations. Other distance measures tested on unlabeled ribs exhibit relatively high average reconstruction errors and lack accuracy.

The evaluation on real X-ray images of the phantom, from which the segmentation was obtained manually, also reveal accuracies (rotation errors $\leq 0.4°$) suitable to detect undesirable pose differences between image pairs, although only a single PA-projection was available for each reconstruction. It was even shown that it is possible to obtain visually plausible reconstructions from real clinical X-ray images. A *symmetric* distance measure on labeled ribs is the appropriate choice, when reconstructions are performed from one real X-ray image.

7.1.2 Accuracy of Shape Reconstruction

The direct 3D surface optimization experiment of pose independent shape reconstructions (pose parameters are known in advance, see Sect. 6.2.5) shows that a considerable part of the reconstruction error is due to the limitation of the SSM's model space. The cause of the residual error is presumably the mutual occlusion of the ribs in the projection data. The accuracies of the pose independent shape reconstruction for all distance measures on labeled and unlabeled ribs are close to the results of the direct 3D surface optimization. Thus, all distance measures are applicable. The results are comparable to those achieved in the work of Lamecker

et al. [LWH06] for the reconstruction of the pelvis (2.6 mm mean surface distance), despite of the geometrically more demanding shape of the rib cage.

The experiments on the pose independent recovery of the shape reveal the capability of the SSM to reconstruct an unknown shape from projection images using our method. In a realistic reconstruction of an unknown patient-specific rib cage, the pose parameters need to be estimated simultaneously with the shape. For this combined shape and pose recovery, all the tested distance measures are suitable in case the ribs are *labeled*. The reconstruction errors range from 2.2 to 2.9 mm, i.e., they are only 0.1 to 0.7 mm worse than the pose independent shape reconstructions. The error in the pose parameters ranges between 0.2° and 1.1°. Thus, the pose is also accurately estimated during combined shape and pose reconstructions on labeled ribs.

Robust reconstruction results on combined shape and pose reconstruction with *unlabeled* ribs can only be obtained with one of the distance measures tested (D_S, d_a). Due to the initialization procedure and the incorporation of the contour normals into the distance measure, global mis-assignments of ribs and contour mismatches are avoided. However, the accuracy of reconstructions with unlabeled ribs is lower then with labeled ribs. A possible reason for this inaccuracy is that for a combined reconstruction of the shape and pose we initially fit the average shape $\overline{\mathbf{v}}$ to the image data. Thereby the final pose of the shape yet to be reconstructed is only roughly approximated. However, small deviations from the correct pose can cause mis-adaptations of the model driven by the adaptation of the shape weights $\mathbf{b}$, especially if point correspondences between silhouettes are not constrained by a labeling of the ribs. In some cases on unlabeled ribs, using D_S with d_a, this leads to local mis-adaptations, that diminish the overall reconstruction quality (cf. Fig. 6.10(b)).

There is still some room for improving the accuracy and robustness of combined shape and pose reconstruction with regard to the optimization approach as well as the optimal choice of the parameters involved in the reconstruction process. One idea is to use stochastic optimization methods to analyze the non-convexity of the distance measures. With this we may gain insight for developing multilevel optimization strategies, which are both efficient and able to overcome local minima. We have already performed first experiments with a sequential consideration of the shape parameters (multi-level strategy, cf. Sect. 4.5.2). This improves the accuracy of the 3D shape reconstruction from an average surface distance of 4.7 ± 2.4 mm (max. 12 mm) to 4.4 ± 0.8 mm (max. 5.5 mm). In future work such strategies should be investigated systematically.

Table 7.1: Simplified overview of the method's performance, classified according to the different reconstruction tasks and the number of views used. Rating criteria are the accuracy achievable and the applicability of the different distance measures (e.g. the use of distance measure D_A is higher rated than D_S).

Rib segmentation	Pose		Shape	Pose + Shape
	PA	PA/lateral	PA/lateral	PA/lateral
Labeled	+++	+++	+++	+++
Unlabeled	++	+++	++	+

7.1.3 Comparison with Other Methods

To the best of our knowledge, there are no other methods that quantify pose reconstruction of the 3D rib cage from 2D projections. Bhunre et al. [BLH07] recover the pose of the distal and proximal femur from one 2D image within an experimental setup that is similar to ours. They also measure the accuracy of their method by assessing the angular error using Euler angles and achieve results of 0.8° to 2.3° on average, where the method proposed in this work obtains clearly more accurate results (0.1° to 0.4°) for the rib cage from one PA-view.

Most existing reconstruction methods for the reconstruction of the rib cage's shape do not obtain a reconstruction of the rib cage surface, but 3D models of rib midlines. Moreover, they mainly assess their reconstruction qualities not directly but via derived quantities, such as chord length or maximal curvature [BLP+08, DS88, DPdG+03, MZB+08]. For our application, these measures are not well suited, since the objective is to globally recover the shape of a patient-specific rib cage as accurately as possible, to be subsequently used for pose reconstructions.

Benameur et al. [BMDDG05] validated their rib cage reconstruction method only against another method [DS88], and not against some reliable ground truth, as in our case. By comparison, the method presented in this thesis uses surfaces extracted from CT-data, which serves as a more reliable gold standard. The mean 3D distance between reconstructed model to the reference midline model is 1.6 mm on average [BMDDG05], where the method proposed in this thesis yields surface distances from 2.2 to 4.7 mm, depending on the distance measure chosen. Since the 3D surface distance is computed between *corresponding* points of the reconstructed model and the reference surface, the accuracies are comparable. However, measuring the 3D distance between midlines is less sensitive against surface deviations than measuring the surface distance directly, and hence is expected to generally provide better results. The method of Dansereau et al. [DS88] achieves an accuracy of 1 mm. This value is determined from radiographs of 7 isolated ribs by means of radio-opaque markers.

7.2 Application to the Clinics

The proposed reconstruction method permits to obtain reconstructions of the 3D pose and shape of the rib cage within a well-defined experimental setup, i.e., from artificial binary projection images. This provides a solid basis and premise for future clinical applications. Beyond that, it was already shown in Sect. 6.3 that is possible to perform pose reconstructions from real X-ray images, even from one PA-image only.

3D Pose Difference improving Subtraction Images The goal and task of this thesis was to render the determination of 3D pose differences between projection images possible. Given two projection images, one previous image with a rib cage's pose $T_{previous}$ and another follow up image acquired with different pose of the rib cage $T_{followUp}$, then the 3D pose difference is defined by

$$T_{3D\_diff} = T_{previous} \cdot T_{followUp}^{-1}. \tag{7.1}$$

The assessment of $T_{previous}$ and $T_{followUp}$ is possible and can be achieved with the accuracies stated in the previous section.

The reconstruction method devised in this thesis is a module of a CAD system (cf. Fig. 2.6 in Sect. 2.3) for detecting interval changes by means of temporal image subtraction. This module contributes 3D information to an image registration process, that normally relies only on the 2D information from the 2D images, in order to improve the subtraction quality. The evaluation of the entire CAD system, and with this the assessment to which degree the 3D information contributes to an improvement of the image subtraction, is beyond the scope of this thesis. This is why the requirements for the pose reconstruction are difficult to define as it is not clear yet which accuracy is needed to improve the quality of the image subtraction with respect to the detection of interval changes within a clinical setting.

Nevertheless, it is already beneficial to know up to what 3D pose differences between previous and follow up image interval changes are still detectable using present 2D to 2D image registration approaches. To this end, von Berg et al. [vBMSPN08] performed a phantom study. They conclude that interval changes are detectable up to cut-off angles of 4.1° with non-deformable registration. Based on the study, von Berg et al. reason that by using their deformable 2D to 2D registration approach the cut-off angle is increased by 2.3° (to 6.4°). Although these cut-off angles are specific to the nature and size of the interval change and, thus, do not generally apply, they can serve as an indicator for the range of 3D pose difference in which conventional 2D to 2D registration approach can yield acceptable subtraction results.

Since the presented method allows for pose reconstruction of well below 1°, it can be utilized to assess whether it is worthwhile to apply an image subtraction using 2D to 2D registration, or if the 3D pose difference is to high to generate a reasonable subtraction image. This way, difficult cases can be at least detected and sorted out. In general, the 3D information gained in the pose reconstruction process can be applied to improve the subtraction procedure, though the improvement achievable depends on the actual subtraction technique and how it processes the additional 3D information. This is of particular interest for high 3D pose deviations ($\geq 6.4°$ according to the study in [vBMSPN08]), because here the existing subtraction approach using deformable 2D to 2D registration can not be applied.

From a clinical point of view, there are two important issues that should be addressed in future work to render the current approach fully available to a clinical application:

Segmentation of the Ribs Throughout this work, it has been assumed that silhouettes of the ribs can be identified in the radiographs. In real PA-radiographs it is possible to manually segment the ribs up to a certain accuracy. The task is tedious, thus, an automation is desirable. In practice, however, it is difficult to automatically detect the ribs in radiographs, especially in lateral images. Therefore, two directions for future research are anticipated.

One is to enable the detection of ribs in radiographs. A promising approach that allows for the extraction of posterior and anterior ribs from PA-images was presented by Plourde et al. [PCD06]. The other one is to investigate how to extend the distance measure to deal with incomplete input data, which is likely to be produced by rib detection methods. We have presented first experiments using asymmetric

distance measures, which suggest that incomplete silhouettes, e.g., arising from edge detecting methods, may also lead to good results. Moreover, the results of the pose reconstruction from radiographs indicate that robust reconstructions are feasible despite incomplete manual segmentations.

Shape Reconstruction from Clinical Radiographs A current limitation of the present approach is the need for two *calibrated* biplanar projection images to obtain a simultaneous reconstruction of the shape and pose. Although in clinical routine a PA and a lateral image is acquired, the spatial relation between both is unknown, since the patient turns approximately 90° for the lateral image. Since PA and lateral image do not represent the same scene, a shape and pose reconstruction from one PA-image only is desirable. However, it was shown that this is not possible (cf. Sect. 6.2.5).

In future research, the method needs to be extended to shape reconstruction from two 'uncalibrated' radiographs. An idea is to optimize two separate sets of pose parameters, one for each images, and one mutual set of shape parameters for both images to retrieve the shape. Furthermore, since the segmentation of the ribs in lateral images is difficult, other information as the boundary of the lung field or the the silhouettes of the vertebrae, which are clearly visible, may be used.

Beside the two essential topics discussed above, it could be tested if an incorporation of more detail into the statistical 3D model improves the performance of the reconstruction method. Similar to the approach of Yao and Taylor [YT00] information about the bone densities encoded in a shape model could be used to generate more sophisticated model projections. The adaptation of the model would then not only rely on the comparison of silhouettes, but also on the intensities within the projection images.

8 Conclusions

In this thesis, the fundamental problem of reconstructing the 3D pose and shape of the human rib cage from 2D projection images has been investigated. The proposed method minimizes deviations between silhouettes of a projected 3D statistical shape model and silhouettes of the ribs in radiographs.

We could show that with several different approaches the 3D shape and pose of the rib cage can be accurately estimated under well-defined and reproducible conditions. This demonstrates that the 2D/3D reconstruction problem can be solved and it thus provides a solid foundation for the development of clinical solutions. More specifically, this is an essential step towards the recovery of 3D pose information from radiographs for improving computer-aided diagnosis based on image subtraction of sequences of chest radiographs.

This work is based on the assumption that the ambiguous and ill-posed 2D/3D reconstruction problem can be solved by the incorporation of a-priori knowledge. Statistical shape models have proven to be a suitable instrument in this context by providing robustness through knowledge on inter-individual shape variability. Furthermore, the combined use of different information from radiographs, e.g., features like edges and gradients, or the annotation of individual ribs, is an effective concept. While the use of edge-based features turned out to be efficient for the purpose of this work, an interesting future approach could be to combine intensity-based and feature-based techniques to obtain a higher reconstruction accuracy. In addition, good initialization strategies can often compensate limited information in the radiographs and prevent erroneous reconstructions.

To achieve unsupervised pose and shape reconstructions from clinical data, two important directions of future work need to be addressed: First, an approach to segment the ribs in radiographs automatically needs to be devised. Second, since a shape reconstruction from a single PA-radiograph is not possible and ribs in lateral radiographs are hard to identify, the method has to be adapted to cope with shape reconstruction based on two clinical radiographs (PA and lateral).

Concerning the application to temporal image subtraction, there are several open issues: It remains to be tested, if the knowledge about a 3D pose difference leads to an improvement of subtraction images and if the accuracy obtained is sufficient. In addition, the claim that a rib cage can be reconstructed once and then subsequently used to assess its pose in different radiographs needs to be verified. It is based on the assumption, that the bone assembly of ribs hardly changes in shape. However, a possible movement of the individual ribs, e.g., due to respiration, needs to be investigated, since this could introduce new problems and impair the pose reconstruction quality.

This thesis shows that 2D/3D reconstruction problems can be solved through an appropriate modeling of application-specific knowledge. This insight may serve as an inspiration to tackle other applications even beyond the bio-medical field.

Bibliography

[Alt02] W. Alt. *Nichtlineare Optimierung - Eine Einfhrung in Theorie, Verfahren und Anwendungen*. Vieweg Verlag, 2002. 34

[BLH07] P.K. Bhunre, W.K. Leow, and T.S. Howe. Recovery of 3d pose of bones in single 2d x-ray images. *IEEE Workshop on Applications of Computer Vision, WACV '07*, pages 48–48, Feb. 2007. 16, 19, 63

[BLP+08] S. Bertrand, S. Laporte, S. Parent, W. Skalli, and D. Mitton. Three-dimensional reconstruction of the rib cage from biplanar radiography. *IRBM*, 29(4):278 – 286, 2008. 12, 13, 14, 20, 63

[BM92] P.J. Besl and H.D. McKay. A method for registration of 3-d shapes. *IEEE Transactions on Pattern Analysis and Machine Intelligence*, 14(2):239–256, Feb 1992. 15, 19

[BMDDG05] S. Benameur, M. Mignotte, F. Destrempes, and J.A. De Guise. Three-dimensional biplanar reconstruction of scoliotic rib cage using the estimation of a mixture of probabilistic prior models. *Biomedical Engineering, IEEE Transactions on*, 52(10):1713–1728, Oct. 2005. 14, 15, 17, 30, 63

[BvB09] D. Barthel and J. von Berg. Robust automatic lung field segmentation on digital chest radiographs. *Int J CARS*, 4(Suppl 1):326–327, 2009. 40

[CKSK00] C.M. Cyr, A.F. Kamal, T.B. Sebastian, and B.B. Kimia. 2d-3d registration based on shape matching. *IEEE Workshop on Mathematical Methods in Biomedical Image Analysis, Proceedings*, pages 198–203, 2000. 16

[CTCG95] T.F. Cootes, C.J. Taylor, D.H. Cooper, and J. Graham. Active shape models - their training and application. *Comput. Vis. Image Underst.*, 61(1):38–59, January 1995. 17, 27, 29, 30, 35

[Dav02] R.H. Davies. *Learning Shape: Optimal Models for Analysing Natural Variability*. PhD thesis, Division of Imaging Science and Biomedical Engineering, Univ. Manchester, 2002. Three measures for shape correspondence evaluation: Compactness, Generality, Specificity. 30

[DBKS+08] P.W. De Bruin, B.L. Kaptein, B.C. Stoel, J.H. Reiber, P.M. Rozing, and E.R. Valstar. Image-based rsa: Roentgen stereophotogrammetric analysis based on 2d-3d image registration. *J Biomech*, 41(1):155–64, 2008. 16, 18

[DCD+05] J. Dubousset, G. Charpak, I. Dorion, W. Skalli, F. Lavaste, J.A. de Guise, G. Kalifa, and S. Ferey. A new 2d and 3d imaging approach to musculoskeletal physiology and pathology with low-dose radiation and the standing position: the eos system. 2005. 12, 13, 19

[DJ94] M.-P. Dubuisson and A.K. Jain. A modified hausdorff distance for object matching. In *Pattern Recognition, 1994. Vol. 1 - Conference A: Computer Vision & Image Processing., Proceedings of the 12th IAPR International Conference on*, volume 1, pages 566–568 vol.1, Oct 1994. 19

[DLvB+09] J. Dworzak, H. Lamecker, J. von Berg, T. Klinder, C. Lorenz, D. Kainmüller, H. Seim, H.-C. Hege, and S. Zachow. 3d reconstruction of the human rib cage from 2d projection images using a statistical shape model. *International Journal of Computer Assisted Radiology and Surgery, Springer Berlin / Heidelberg*, 2009. 5

[DMX+97] M.C. Difazio, H. MacMahon, X.W. Xu, P. Tsai, J. Shiraishi, S.G. Armato, and K. Doi. Digital chest radiography: effect of temporal subtraction images on detection accuracy. *Radiology*, 202(2):447–452, 1997. 10

[DPdG+03] S. Delorme, Y. Petit, J.A. de Guise, H. Labelle, C.-E. Aubin, and J. Dansereau. Assessment of the 3-d reconstruction and high-resolution geometrical modeling of the human skeletal trunk from 2-d radiographic images. *IEEE Transactions on Biomedical Engineering*, 50(8):989–998, Aug. 2003. 13, 14, 19, 21, 63

[DS88] J. Danserau and I.A.F. Srokest. Measurements of the three-dimensional shape of the rib cage. *J. Biomech.*, 21:893–901, 1988. 13, 14, 15, 63

[FAB95] J. Feldmar, N. Ayache, and F. Betting. 3d-2d projective registration of free-form curves and surfaces. In *ICCV95*, page 549, 1995. 16, 19

[FL99] M. Fleute and S. Lavallée. Nonrigid 3-d/2-d registration of images using statistical models. In *MICCAI '99: Proceedings of the Second International Conference on Medical Image Computing and Computer-Assisted Intervention*, pages 138–147, London, UK, 1999. Springer-Verlag. 16, 17, 19, 20, 30

[Gow75] J. Gower. Generalized procrustes analysis. *Psychometrika*, 40(1):33–51, March 1975. 28

[HSK08] E. Hekmatian, S. Sharif, and N. Khodaian. Literature review digital subtraction radiography in dentistry. *Dental Research Journal*, 2(2), 2008. 10

[HZ04] R. Hartley and A. Zisserman. *Multiple View Geometry in Computer Vision*. Cambridge University Press, March 2004. 30

[JKT+02] T. Johkoh, T. Kozuka, N. Tomiyama, O. Hamada, S.and Honda, N. Mihara, M. Koyama, M. Tsubamoto, M. Maeda, H. Nakamura, H. Saki, and K. Fujiwara. Temporal subtraction for detection of solitary pulmonary nodules on chest radiographs: Evaluation of a commercially available computer-aided diagnosis system1. *Radiology*, 223(3):806–811, 2002. 10

[Jol02] I.T. Jolliffe. *Principal Component Analysis*. Springer, October 2002. 28

[KDM+94] A. Kano, K. Doi, H. MacMahon, D.D. Hassell, and M.L. Giger. Digital image subtraction of temporally sequential chest images for detection of interval change. *Medical Physics*, 21(3):453–461, 1994. 1, 49

[KKH+06] S. Kakeda, K. Kamada, Y Hatakeyama, T. Aoki, Y. Korogi, S. Katsuragawa, and K. Doi. Effect of temporal subtraction technique on interpretation time and diagnostic accuracy of chest radiography. *Am. J. Roentgenol.*, 187(5):1253–1259, 2006. 1, 10

[KLL07] D. Kainmüller, T. Lange, and H. Lamecker. Shape constrained automatic segmentation of the liver based on a heuristic intensity model. *Proc. MICCAI Workshop 3D Segmentation in the Clinic: A Grand Challenge*, pages 109–116, 2007. 30

[KLvB+07] T. Klinder, C. Lorenz, J. von Berg, S.P.M. Dries, T. Bülow, and J. Ostermann. Automated model-based rib cage segmentation and labeling in ct images. In *MICCAI 2007, Part II*, pages 195–202. LNCS 4792, 2007. 35

[KWG09] C. Koehler, T. Wischgoll, and F. Golshani. 3-d reconstruction of the human ribcage based on chest x-ray images and geometric template models. *IEEE MultiMedia, IEEE computer Society Digital Library*, Sept. 2009. Accepted for future publication. 15

[KYM+99] Y. Kurihara, Y.K. Yakushiji, J. Matsumoto, T. Ishikawa, and K. Hirata. The ribs: Anatomic and radiologic considerations. *Radiographics*, 19(1):105–119, 1999. 9

[Lam08] H. Lamecker. *Variational and statistical shape modeling for 3D geometry reconstruction*. Ph.d. thesis, Freie Universität Berlin, Fachbereich Mathematik und Informatik (P. Deuflhard), October 2008. 28, 30

[LMVS03] D. Loeckx, F. Maes, D. Vandermeulen, and P. Suetens. Temporal subtraction of thorax cr images using a statistical deformation model. *IEEE Transactions on Medical Imaging*, 22:1490–1504, 2003. 10

[LS95] S. Lavallée and R. Szeliski. Recovering the position and orientation of free-form objects from image contours using 3d distance maps. *IEEE Transactions on Pattern Analysis and Machine Intelligence*, 17(4):378–390, 1995. 16, 17, 19, 20

[LSDG+03] S. Laporte, W. Skalli, J.A. De Guise, F. Lavaste, and D. Mitton. A biplanar reconstruction method based on 2d and 3d contours: application to the distal femur. *Comput. Methods Biomech. Biomed. Eng.*, 6(1):1–6, 2003. 20

[LvG06] M. Loog and B. van Ginneken. Segmentation of the posterior ribs in chest radiographs using iterated contextual pixel classification. *IEEE Transactions on Medical Imaging*, 25(5):602–611, May 2006. 4, 12

[LWH06] H. Lamecker, T.H. Wenckebach, and H.C. Hege. Atlas-based 3d-shape reconstruction from x-ray images. In *Proc. Int. Conf. of Pattern Recognition (ICPR2006)*, volume 1, pages 371–374, 2006. 4, 6, 16, 17, 19, 21, 30, 36, 62

[Mar76] G. T. Marzan. *Rational design for close-range photogrammetry*. PhD thesis, Dept. Civil Eng., Univ. Illinois at Urbana-Champaign, 1976. 13

[MBF+06] M. Mahfouz, A. Badawi, E.E.A. Fatah, M. Kuhn, and B. Merkl. Reconstruction of 3d patient-specific bone models from biplanar xray images utilizing morphometric measurements. In *Proc. Int. Conf. on Image Processing, Computer Vision and Pattern Recognition (IPCV)*, volume 2, pages 345–349, 2006. 16, 17, 30

[MNV99] E.H.W. Meijering, W.J. Niessen, and M.A. Viergever. Retrospective motion correction in digital subtraction angiography: A review. *IEEE Trans. Med. Imaging*, 18(18):2–21, 1999. 10

[MZB+08] D. Mitton, K. Zhao, S. Bertrand, C. Zhao, S. Laporte, C. Yangb, K.-N. Anb, and W. Skallia. 3d reconstruction of the ribs from lateral and frontal x-rays in comparison to 3d ct-scan reconstruction. *Journal of Biomechanics*, 41:706–710, 2008. 13, 14, 20, 63

[NCPL04] J. Novosad, F. Cheriet, Y. Petit, and H. Labelle. Three-dimensional (3-d) reconstruction of the spine from a single x-ray image and prior vertebra models. *IEEE Transactions on Biomedical Engineering*, 51(9):1628–1639, Sept. 2004. 13, 19

[PCD06] F. Plourde, F. Cheriet, and J. Dansereau. Semi-automatic detection of scoliotic rib borders using chest radiographs. In *Studies in Health Technology and Informatics Vol. 123 (IRSSD 2006)*, pages 533–537, 2006. 4, 12, 15, 64

[PJW03] M. Park, J.S. Jin, and L.S. Wilson. Detection and labeling ribs on expiration chest radiographs. In J. Martin and L. E. Antonuk, editors, *Medical Imaging 2003: Physics of Medical Imaging, Proceedings of the SPIE*, volume 5030, pages 1021–1031, 2003. 4, 12

[PWL+98] G.P. Penney, J. Weese, J.A. Little, P. Desmedt, D.L.G. Hill, and D.J. Hawkes. A comparison of simularity measures for use in 2d-3d medical image registration. In *MICCAI*, pages 1153–1161, 1998. 18

[RCPA07] M. Roberts, T. Cootes, E. Pacheco, and J. Adams. Quantitative vertebral fracture detection on dxa images using shape and appearance models. *Academic radiology*, 14(10):1166–1178, 2007. 30

[RL01] S. Rusinkiewicz and M. Levoy. Efficient variants of the icp algorithm. *3-D Digital Imaging and Modeling, 2001. Proceedings. Third International Conference on*, pages 145–152, 2001. 20

[Roh00] T. Rohlfing. *Multimodale Datenfusion für die bildgesteuerte Neurochirurgie und Strahlentherapie*. PhD thesis, Technische Universität Berlin, 2000. 33

[Rön95] W.C. Röntgen. Über eine neue art von strahlen. *Aus den Sitzungsberichten der Wrzburger Physik.-medic. Gesellschaft*, 1895. 8

[Ruc97] W.J. Rucklidge. Efficiently locating objects using the hausdorff distance. *Int. J. Comput. Vision*, 24(3):251–270, 1997. 19

[SCT06] O. Sadowsky, J.D. Cohen, and R.H. Taylor. Projected tetrahedra revisited: A barycentric formulation applied to digital radiograph reconstruction using higher-order attenuation functions. *IEEE Transactions on Visualization and Computer Graphics*, 12(4):461–473, 2006. 18

[SFK+08] P. Steininger, K.D. Fritscher, G. Kofler, B. Schuler, M. Hänni, K. Schwieger, and R. Schubert. Comparison of different metrics for appearance-model-based 2d/3d-registration with x-ray images. pages 122–126, 2008. 18

[Shl05] J. Shlens. A tutorial on principal component analysis - version 2. December 2005. Unpublished. http://www.brainmapping.org/NITP/PNA/Readings/pca.pdf. Last visited 22.10.2009. 28

[SKH+08] H. Seim, D. Kainmueller, M. Heller, H. Lamecker, S. Zachow, and H.-C. Hege. Automatic segmentation of the pelvic bones from ct data based on a statistical shape model. In *Eurographics Workshop on Visual Computing for Biomedicine (VCBM)*, pages 93–100, Delft, Netherlands, 2008. 30

[TJK+02] M. Tsubamoto, T. Johkoh, T. Kozuka, N. Tomiyama, S. Hamada, O. Honda, N. Mihara, M. Koyama, M. Maeda, H. Nakamura, and K. Fujiwara. Temporal subtraction for the detection of hazy pulmonary opacities on chest radiography. *Am. J. Roentgenol.*, 179(2):467–471, 2002. 10

[vBMSPN08] J. von Berg, D. Manke, C. Schaefer-Prokop, and U. Neitzel. Impact of patient pose differences on subtle interval change detection by temporal subtraction in chest radiographs. a phantom study. In *European Radiology*, volume 18 suppl. 1 of *Proc of ECR 2008*, page 212, 2008. 1, 56, 64

[vGtHR00] B. van Ginneken and B.M. ter Haar Romeny. Automatic delineation of ribs in frontal chest radiographs. In *Proceedings of the SPIE*, volume 3979, pages 825–836, 2000. 4, 12

[vGtHRV01] B. van Ginneken, B.M. ter Haar Romeny, and M.A. Viergever. Computer-aided diagnosis in chest radiography: a survey. *IEEE Transactions on Medical Imaging*, 20(12):1228–1241, Dec. 2001. 1

[WRK+87] T.A. Wilson, K. Rehder, S. Krayer, E.A. Hoffman, C.G. Whitney, and J.R. Rodarte. Geometry and respiratory displacement of human ribs. *J Appl Physiol*, 62(5):1872–1877, May 1987. 8

[Yao02] J. Yao. *A statistical bone density atlas and deformable medical image registration*. PhD thesis, Johns Hopkins University,, Baltimore, Maryland, 2002. Adviser: R.H. Taylor. 18

[YGA95] Z. Yue, A. Goshtasby, and L.V. Ackerman. Automatic detection of rib borders in chest radiographs. *IEEE Transactions on Medical Imaging*, 14(3):525–536, Sep 1995. 4, 12

[YT00] J. Yao and R.H. Taylor. Tetrahedral mesh modeling of density data for anatomical atlases and intensity-based registration. In *MICCAI '00: Proceedings of the Third International Conference on Medical Image Computing and Computer-Assisted Intervention*, pages 531–540, London, UK, 2000. Springer-Verlag. 18, 65

[YWN+04] T. Yamazaki, T. Watanabe, Y. Nakajima, K. Sugamoto, T. Tomita, H. Yoshikawa, and S. Tamura. Improvement of depth position in 2-d/3-d registration of knee implants using single-plane fluoroscopy. *IEEE transactions on medical imaging*, 23(5):602–612, May 2004. 16, 19

[ZA] Visualisation Software ZIB-Amira. http://amira.zib.de/. 5

[ZGS+09] G. Zheng, S. Gollmer, S. Schumann, X. Dong, T. Feilkas, and M.A. Gonzalez Ballesterac. A 2d/3d correspondence building method for reconstruction of a patient-specific 3d bone surface model using point distribution models and calibrated x-ray images. *Medical Image Analysis*, In Press, Corrected Proof, 2009. 21

[Zhe06] G. Zheng. Reconstruction of patient-specific 3d bone model from biplanar x-ray images and point distributionmodels. In *ICIP06*, pages 1197–1200, 2006. 16, 17, 19, 30

[ZLES05] S. Zachow, H. Lamecker, B. Elsholtz, and M. Stiller. Reconstruction of mandibular dysplasia using a statistical 3d shape model. In eds. H. Lemke et al, editor, *Proc. Computer Assisted Radiology and Surgery (CARS)*, Int. Congress Series (1281), pages 1238–1243. Elsevier, 2005. 30